Inclusive open charm photoproduction in ultraperipheral collisions at the LHC with in the generalized photon-nucleus fixed-order next-to-leading logarithm framework

Matteo Cacciari,[1,2] Gian Michele Innocenti,[3] and Anna M. Staśto[4]

[1]*Sorbonne Université, CNRS, Laboratoire de Physique Théorique et Hautes Énergies, LPTHE, F-75005 Paris, France*

[2]*Université Paris Cité, LPTHE, F-75006 Paris, France*

[3]*Massachusetts Institute of Technology, Cambridge, Massachusetts 02139, USA*

[4]*Department of Physics, Penn State University, University Park, Pennsylvania 16802, USA*

(Received 22 June 2025; accepted 22 October 2025; published 18 November 2025)

We compute the inclusive D^0 production cross section in ultraperipheral Pb-Pb collisions at the LHC as a function of the D^0 transverse momentum and rapidity. These calculations are carried out within the new generalized photon-nucleus FONLL (GγA-FONLL) framework, which can predict photonuclear cross sections for charm and beauty hadrons in electron-proton, electron-nucleus, and ultraperipheral heavy-ion collisions. The framework relies on fixed-order next-to-leading logarithm (FONLL) to model heavy-quark production in photonuclear collisions and employs a photon-flux reweighting procedure to describe the production cross sections in ultraperipheral heavy-ion collisions. The GγA calculations are first validated against the photoproduction cross sections of D^* in electron-proton collisions at HERA. The predictions for the D^0 production cross section in ultraperipheral Pb-Pb collisions at the LHC are then presented and compared to the first experimental results obtained by CMS at $\sqrt{s_{\mathrm{NN}}} = 5.36$ TeV. The predictions are benchmarked against different choices of nuclear parton distribution functions, fragmentation functions, and renormalization and factorization scales.

DOI: 10.1103/1w13-r2tr

I. INTRODUCTION

Ultraperipheral collisions (UPCs) of nuclei at very high energies provide unique opportunity to characterize the properties of nuclear structure, and perform tests of perturbative quantum-chromo dynamics (QCD) in a clean experimental environment [1–3]. In UPCs, two Lorentz-contracted nuclei scatter at impact parameters that exceed the sum of the radii of the two nuclei. As a result, UPCs are dominated by electromagnetic processes, while hadronic scatterings are suppressed. At high energies, the strong electromagnetic fields surrounding the ultrarelativistic ions can be viewed as a flux of quasireal photons, which is calculable thanks to the use of the equivalent photon approximation (EPA) method [4–7]. UPCs lead to large cross sections for photonuclear interactions. For processes involving heavy-quark production, the cross sections can be calculated using standard collinear factorization theorems in terms of perturbatively calculable partonic cross sections and nuclear parton distribution functions (nPDF) (see for example [8]).

Extensive experimental [9–13] and theoretical [14–24] efforts have been devoted to the study of charmonium production in UPCs. In particular, measurements of the exclusive production of J/ψ mesons in coherent photon-Pb scatterings [9–13] have provided experimental indications of a strong suppression of the lead PDF for gluons at very small values of x. Despite the unprecedented low-x coverage, the constraining power of these observables remains limited by the complex theoretical description of coherent J/ψ photoproduction and by the fact that these measurements probe gluon density at scales restricted to the mass of the vector meson.

The study of "open" heavy-flavor (charm and beauty) production in UPCs offers an outstanding opportunity to extend the experimental constraints into unexplored kinematic regimes. To date, theoretical calculations of heavy quark production in ultraperipheral collisions (UPCs) have been performed only at leading order, either within collinear factorization [23,25–27] or using the color glass condensate framework [27,28]. Charmed hadrons such as D^0 and D^*, produced in photonuclear reactions, can be exploited as powerful probes of nuclear structure. Since both the hard scale and the parton momentum fraction

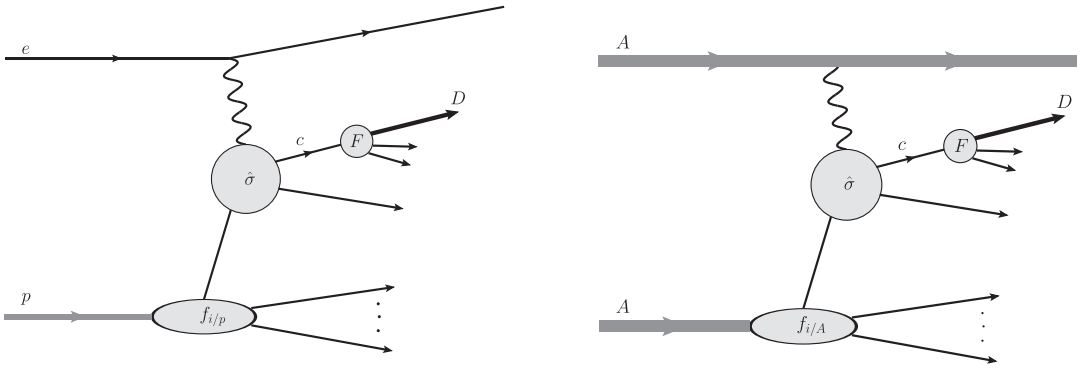

FIG. 1. Schematic description of the inclusive D meson production in electron-proton collisions (left) and in ultraperipheral heavy-ion collisions (right). Here: $f_{i/p}$ and $f_{i/A}$ denotes PDF in the proton or nucleus, F fragmentation function and $\hat{\sigma}$ hard scattering process.

(Bjorken-x) can be inferred from the transverse momenta and rapidity of the final-state charm quarks, measurements of charmed-meson cross sections as a function of p_T and rapidity (y) provide unique constraints on the gluon properties in the nucleus across various x and Q^2 regimes. While the photoproduction of D^* mesons was extensively measured in electron-proton collisions at HERA [29–31], it is only recently that the feasibility of similar measurements in UPCs has been demonstrated. The CMS Collaboration presented the first analysis [32] of inclusive D^0 production in ultraperipheral PbPb collisions at $\sqrt{s_{\mathrm{NN}}} = 5.36$ TeV. The measurement, carried out as a function of p_T and y in the ranges $2 < p_T < 12$ GeV and $-2 < y < 2$, is sensitive the gluon density in the nucleus for scales in the region $Q^2 \simeq 30$–200 GeV^2 and for values of x down to about 10^{-3} (see II B for more detail). These new experimental opportunities underscore the need for accurate theoretical calculations to describe open charm and beauty production in UPCs and in high-energy electron-ion collisions at the Electron-Ion Collider [33,34] as well as in proposed facilities, such as Large Hadron electron Collider (LHeC) [35,36].

In the present work, we compute the inclusive D^0 production cross section in ultraperipheral PbPb collisions at the LHC using the newly developed generalized-photon-nucleus fixed-order next-to-leading logarithm (GγA-FONLL) framework. It generalizes the calculation of photonuclear heavy-flavor production implemented in FONLL for electron-proton and electron-nucleus to UPCs. The fixed-order next-to-leading logarithm (FONLL) framework [37,38] is used to compute the photoproduction of charm in the fixed next-to-leading order (FO) and fixed order plus next-to-leading logarithmic enhancements of $\ln \frac{p_T}{m}$ at high p_T. Since the photoproduction of charm was extensively measured at the HERA collider, we have validated our calculations against data from the H1 [29,31] and ZEUS [30] experiments. As part of this validation, the earlier FONLL calculations from [39] were updated with the latest parton distribution functions for protons (PDFs). The framework developed to reproduce charmed-meson cross sections in electron-proton collisions was subsequently adapted to describe the corresponding cross sections measured in UPCs. Although photoproduction processes in UPCs are in many ways analogous to those in electron-proton and electron-ion collisions, important differences remain (see Fig. 1). The most evident difference is the photon flux in electron-nucleus versus electron-proton collisions. Although the flux from the nucleus is enhanced by square of the atomic number Z, its functional dependence on the photon energy differs significantly, producing a generally softer photon spectrum than in the electron case. To account for this distinction, our calculations are modified to reflect the photon flux expected in nuclear collisions. Additional differences arise from the experimental strategy used to select clean photonuclear events in UPCs. The event selection applied in UPCs includes the condition that one of the two colliding nuclei breaks up and the other remains intact (Xn0n) by using the information provided by the zero-degree calorimeters (ZDCs). The 0n requirement means that the event is not fully inclusive unlike theoretical calculation of photoproduction. In addition, the presence of soft electromagnetic interactions between the two colliding nuclei can lead to breakup of the photon-emitting nucleus, leading to a reduction the rate of selected Xn0n events. To allow for a direct comparison with the data, a dedicated correction was computed assuming the factorization of the soft-electromagnetic interactions and the hard scattering.

The Xn0n selection further requires at least one neutron in the opposite ZDC, which partially suppresses diffractive production in the data. Since the nuclear diffractive component is included in the theoretical calculation of inclusive charm production, it is important to note that this component is partially removed in the measurement. A rough estimate based on nuclear diffractive parton distributions from the Frankfurt-Guzey-Strikman model [40] suggests that this effect amounts to about a 10% contribution in the relevant kinematic range. However, a more detailed study

of the diffractive component goes beyond the scope of the present analysis.

The paper is organized as follows: Section II describes the main ingredients of the theoretical calculation of the photoproduction cross section in electron-proton collisions and its extension to ultraperipheral heavy-ion collisions (UPCs). In Sec. III, the resulting predictions for photoproduction in electron-proton collisions at HERA are presented and compared to H1 and ZEUS measurements. Section IV provides the GγA-FONLL predictions for D^0 production in UPCs, and these predictions are then confronted with recent CMS measurements in Sec. V. Finally, our conclusions are presented in Sec. VI, where prospects for future theoretical and experimental efforts are also discussed. In the Appendix we include additional plots with calculations for UPCs.

II. GENERALIZED γA FONLL FRAMEWORK FOR PHOTONUCLEAR CHARM PRODUCTION

The results presented in this paper are obtained within the new GγA-FONLL framework for photonuclear charm photoproduction. This framework has been developed to provide a comprehensive description of heavy-flavor hadron production in photon-proton, photon-nucleus, and ultraperipheral heavy-ion collisions. In particular, it calculates photoproduction cross sections using standard collinear factorization theorems in terms of perturbatively calculable partonic cross sections, PDFs, and fragmentation functions. To ensure consistency with UPC measurements, the calculations are modified to incorporate the softer photon flux expected in nuclear collisions and to account for the experimental strategies used to select clean photonuclear events at colliders. In this section, a detailed description of each ingredient is provided, including a separate subsection that covers the strategy adopted to account for the bias introduced in UPCs by soft-photon exchanges between the ultrarelativistic ions.

A. Photoproduction cross section for heavy quarks

For the calculation of the differential photoproduction cross section for heavy quarks we use the code for the FONLL calculation [38]. In that work a resummation approach was developed which allows for the description of the transverse momentum distribution of heavy quarks produced in photoproduction on a proton or nuclear target. The FONLL approach connects the region of small transverse momenta where the fixed order approach is valid to the region with large transverse momenta where the logarithmically enhanced terms are resummed. To be precise the formalism includes terms up to NLO order, that is terms $\alpha_{\rm em}\alpha_s$ and $\alpha_{\rm em}\alpha_s^2$. These terms are included exactly, with mass effects. In addition, all logarithmically enhanced terms $\alpha_{\rm em}\alpha_s(\alpha_s \ln(p_T/m))^k$ and $\alpha_{\rm em}\alpha_s^2(\alpha_s \ln(p_T/m))^k$ are included, with the possible exception of terms that are suppressed by powers of m/p_T. The matching resummed FONLL cross section can be expressed as [38,39]

$$\text{FONLL} = \text{FO} + (\text{RS-FOM0}) \times G(m, p_T). \tag{1}$$

In this formula the FO is fixed order, that is exact NLO calculation [41,42]. RS is the resummed result with all the logarithmically enhanced contributions, up to terms suppressed by powers of m/p_T. FOM0 is the massless limit of fixed order FO without terms suppressed by powers of m, while logarithms of the mass are retained. Finally, $G(m, p_T)$ is an arbitrary damping function, that must be regular in p_T, and must approach unity up to terms suppressed by powers of m/p_T at large transverse momenta.

The photoproduction cross section contains both *direct* and *resolved* contributions. The direct (or pointlike) contribution has the form

$$\left.\frac{d\sigma}{dydp_T}\right|_{\rm dir} = \sum_j \int dx_p f_{j/H}(x_p) \frac{d\hat{\sigma}_{j\gamma}}{dydp_T}(P_\gamma, x_p P_H), \tag{2}$$

where $f_{j/H}(x_p)$ is the distribution of the parton j in the hadron H and $\frac{d\hat{\sigma}_{j\gamma}}{dydp_T}(P_\gamma, x_p P_H)$ is the partonic cross section for scattering of parton j with photon γ producing a heavy quark in the final state. The resolved (or hadronic) component has the form

$$\left.\frac{d\sigma}{dydp_T}\right|_{\rm res} = \sum_{kj} \int dx_\gamma dx_p f_{k/\gamma}(x_\gamma) f_{j/H}(x_p) \times \frac{d\hat{\sigma}_{kj}}{dydp_T}\left(x_\gamma P_\gamma, x_p P_H\right), \tag{3}$$

where $f_{k/\gamma}$ is the parton density in the photon and $\frac{d\hat{\sigma}_{kj}}{dydp_T}(x_\gamma P_\gamma, x_p P_H)$ is the partonic cross section for scattering of two partons kj resulting with a heavy quark in the final state. In the above we have suppressed the dependence on the factorization and renormalization scales. Both terms given by Eqs. (2) and (3) have expansion as series of $\alpha_{\rm em}\alpha_s^k$ if one takes into account that the parton density in the photon carries a factor $\alpha_{\rm em}/\alpha_s$. It is worth noting that only the sum of direct and resolved contributions is an observable quantity, as both these contributions are related beyond the leading order, see [38].

B. Parametrization of the parton distribution functions for protons and nuclei

For the calculation of the photoproduction cross sections discussed in previous section, which are implemented in the FONLL code, one needs to select the parton distribution function (PDF) for nucleus or a proton. For the

nuclear PDF we take the EPPS21 [43] set as well as the nNNPDF3.0 [44] set. In addition we also perform and compare the calculations with the EPPS21 proton baseline PDF CT18ANLO [45], to estimate the role of the nuclear effects in the kinematics for D^0 production at CMS.

In the EPPS21 [43] set the nuclear modification factor is parametrized and for the baseline proton PDF the CT18ANLO [45] is used. The value of charm mass for this PDF set is $m_c = 1.3$ GeV. The EPPS21 parametrization uses the same datasets as EPPS16 [46] and in addition 5 TeV double-differential CMS dijet and LHCb D-meson data, as well as 8 TeV CMS W boson data from pPb collisions. These new datasets lead to significantly better-constrained gluon distributions at small and intermediate values of the momentum fraction x. In addition new electron-nucleus data from JLab were used in the fit, which impact the large x and small virtualities in the nuclear PDFs. Another improvement in the EPPS21 analysis is the inclusion into the Hessian framework the errors of the baseline proton PDFs and their propagation into the uncertainties of the nuclear PDFs.

The nNNPDF3.0 [44] set extends the NNPDF methodology which uses machine learning methods in the global analysis and extraction of PDFs. In particular the artificial neural networks are used as universal interpolants to parametrize the x and A dependence of the nPDFs. This methodology allows for the reduction of model parametrization bias. The value of charm mass in nNNPDF3.0 is $m_c = 1.5$ GeV. The nNNPDF3.0 set used all the data in the nNNPDF2.0 [47] as well as the additional ones, from the LHC pPb collisions. New datasets included: forward and backward rapidity fiducial cross sections for the production of W bosons at $\sqrt{s} = 5.02$ TeV measured by ALICE experiment; forward and backward rapidity fiducial cross sections for the production of Z bosons measured by ALICE and LHCb at 5.02 TeV and 8.16 TeV; the differential cross section for the production of Z bosons measured by CMS at 8.16 TeV; CMS dijet at 5 TeV and ATLAS prompt photon data at 8.16 TeV and also the LHCb data on D^0 production at 5 TeV. We note that, at present the data on the exclusive J/ψ production in UPC are not used in the global analysis of the nuclear PDFs. Both nPDF sets exhibit very distinctive nuclear modifications of the parton distribution functions. In particular they confirm the presence of shadowing (suppression) of gluons at small x, and antishadowing (enhancement) at large x. For the purpose of benchmarking and comparison of charm production in ep scattering at HERA, presented in Sec. III, we also need to select proton PDFs. For calculation in Sec. III we used CT18ANLO [45] and nNNPDF3.0p [44] which are proton baselines for the EPPS21 and nNNPDF3.0 nuclear PDF sets, respectively. In addition, for the ep case we also performed comparisons using HERAPDF2.0 [48] set.

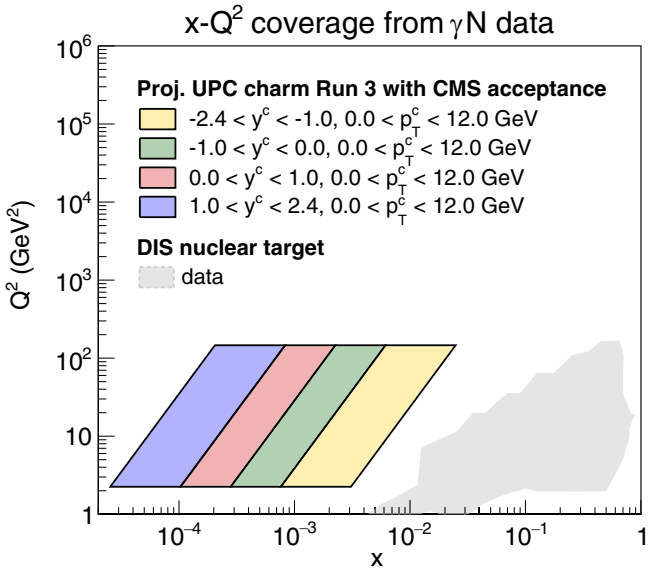

FIG. 2. x and Q^2 coverage charm production in UPCs collisions. In gray, the existing coverage from fixed-target deep-inelastic photonuclear measurements is presented [49].

1. Estimate of the x and Q^2 coverage for D^0 photoproduction measurements

A qualitative estimate of the (x, Q^2) coverage accessible through open-charm observables in ultraperipheral collisions (UPCs) can be obtained by approximating the transverse momentum scale Q^2 with the squared transverse mass of the charm quark $m_T^2 = p_T^2 + m_c^2$ and the target's longitudinal momentum carried by the parton as $x \approx m_T/\sqrt{s_{\rm NN}}e^{-y_c}$, where m_c is the charm quark mass, $\sqrt{s_{\rm NN}}$ is the center-of-mass energy of the nucleon-nucleon system, and p_T is the transverse momentum of the charm quark. In Fig. 2, the predicted (x, Q^2) region probed by open-charm measurements in UPCs at $\sqrt{s_{\rm NN}} = 5.36$ TeV is shown, corresponding to charm-quark transverse momentum in the range $0 < p_{T,c} < 12$ GeV and rapidity $-2.4 < y_c < 2.4$. This kinematic region, which is accessible with existing LHC detectors, enables the exploration of x values from approximately 0.01 down to below 10^{-4}, and Q^2 values ranging from m_c^2 up to around $\sim$100 GeV^2.

C. Photon flux parametrization in electron-proton, electron-nucleus collisions, and PbPb UPCs

In order to compute the cross section in electron-proton collisions at HERA or in UPCs at the LHC, the photoproduction cross section must be convoluted with the photon flux from the electron or the nucleus, respectively. For UPCs, an effective parametrization was developed to account for the geometrical properties of the collisions. To enable direct comparison with experimental measurements, the impact of electromagnetic dissociation on the

photon-emitting nucleus is also taken into account. In this section, a detailed description of the adopted parametrizations in electron-proton, electron-ion and UPCs lead-lead collisions is provided.

D. Photon flux in electron-proton and electron-nucleus collisions

For the description of electron-proton and electron-ion collisions, the original parametrization implemented in the FONLL code was used. The photon flux from electrons implemented in the FONLL code for the electroproduction is given by the following formula

$$f_{\gamma/e}(z) = \frac{\alpha_{em}}{2\pi}\left[\frac{1+(1-z)^2}{z}\log\left(\frac{Q^2_{\max}(1-z)}{(m_e z)^2}\right) + 2m_e^2 z\left(\frac{1}{Q^2_{\max}} - \frac{1-z}{(zm_e)^2}\right)\right]. \quad (4)$$

where z is the fraction of the energy of the electron carried by the photon, m_e is the electron mass, $Q^2_{\max}$ is the limit on the (negative) photon virtuality, and α_{em} is the electromagnetic coupling. The second term in the above expression is a subleading correction, see Ref. [50]. In Fig. 3, the resulting parametrizations for the photon flux from electrons at HERA are shown. The solid black curve corresponds to $Q^2_{\max} = 0.01$ GeV^2, chosen to match the experimental conditions of the *ETAG33* H1 data sample [29]. The dashed blue line uses $Q^2_{\max} = 2$ GeV^2, to enable comparison with the 2012 H1 data [31]. The electron flux is very flat over entire range of z, and has non-negligible dependence on $Q^2_{\max}$. The difference in flux between $Q^2_{\max} = 0.01$ GeV^2 and $Q^2_{\max} = 2$ GeV^2 is of the order of 30 to 60% depending on the fraction of the energy z. We have checked that the second term in Eq. (4) is a small correction of about 3–7% to the leading logarithmic term.

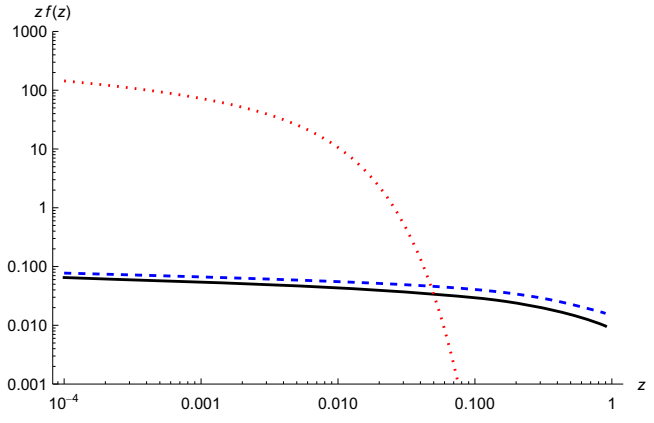

FIG. 3. Photon flux scaled by z as a function of the fractional photon energy z. The electron flux of Eq. (4) is shown for $Q^2_{\max} = 0.01$ GeV^2 (solid black) and $Q^2_{\max} = 2$ GeV^2 (dashed blue), while the lead-nucleus flux of Eq. (5) appears as a red dotted line.

1. Photon flux in ultraperipheral heavy-ion collisions

For the case of the UPCs, the photon flux from electrons was replaced with the expected photon flux from the nucleus. The parametrization considered is the analytic expression presented in [51], obtained in the pointlike approximation

$$f_{\gamma/A}(z) = \int d^2\mathbf{b}\,\tilde{f}_{\gamma/A}(z,\mathbf{b})\theta(|\mathbf{b}| - b_{\min}) = \frac{2Z^2\alpha_{em}}{\pi z}\left[\eta K_0(\eta)K_1(\eta) - \frac{\eta^2}{2}\left(K_1(\eta)^2 - K_0(\eta)^2\right)\right], \quad (5)$$

with the dimensionless variable η defined as

$$\eta = \frac{z m_p b_{\min}}{\hbar c}. \quad (6)$$

In Eq. (5) $\tilde{f}_{\gamma/A}(z,\mathbf{b})$ is the photon flux of the nucleus evaluated at the transverse distance $\mathbf{r} = \mathbf{b}$ where $\mathbf{b}$ is vector connecting the centers of the two nuclei in the transverse plane of the collision. This is appropriate in the pointlike approximation (see for example [52]). Here z is the fraction of the energy of nucleus carried by the photon, m_p is the proton mass, Z atomic number ($Z = 82$ for lead), $b_{\min}$ distance between the nuclei, and K_0, K_1 are modified Bessel functions. Following [52–54] we take the impact parameter $b_{\min} = 2R = 14.2$ fm, with $R = 7.1$ fm being the nuclear hard-sphere radius, to account for the finite size of the colliding nuclei. The parametrization for the photon flux from nuclei, presented in Eq. (5), is shown as a red dotted line in Fig. 3, and compared to the fluxes from electrons at HERA discussed previously. At small z, the photon flux from nuclei is much larger than that from electrons. At intermediate z, it exhibits a sharp cutoff due to the presence of the Bessel functions K_0 and K_1. As a result, the photon flux from nuclei becomes negligible for $z \gtrsim 0.1$. These differences between electron and nucleus fluxes are important when comparing the kinematics of HERA and UPCs at the LHC, as well as when comparing various HERA datasets collected with different kinematic cuts on photon virtuality and z ranges (see Table I in Sec. III).

2. Modeling of the no-break up probability in UPCs

Photonuclear events, in which one of the two colliding nuclei breaks up and the other remains intact, are selected in UPC measurements by requiring that there are no forward neutrons in the zero-degree calorimeter (ZDC) in one direction (0n) and at least one neutron (Xn) in the opposite direction (see Fig. 4). This selection, coupled with the requirement of a large rapidity gap in the photon-going direction, allows for the suppression of the contamination of hadronic events (XnXn) and of two-photon (0n0n) processes.

TABLE I. Kinematic cuts in datasets for D^* photoproduction. Data are from: H1 (*ETAG33* and *ETAG44* scenarios) [29], ZEUS [30] and H1 (2012 data) [31].

Dataset	$Q^2_{\max}$	$z_{\min}$	$z_{\max}$	p_T	(pseudo)rapidity
H1 *ETAG44*	0.009	0.02	0.32	$p_T > 2$ GeV	$\lvert y\rvert < 1.5$
H1 *ETAG33*	0.01	0.29	0.62	$p_T > 2$ GeV	$\lvert y\rvert < 1.5$
ZEUS	1	0.187	0.869	$p_T > 2$ GeV	$\lvert\eta\rvert < 1.5$
H1 2012	2	0.09	0.8	$p_T > 1.8$ GeV	$\lvert\eta\rvert < 1.5$

The presence of a 0nXn requirement, thus, poses some additional difficulties for theoretical calculations. In UPCs, indeed, the presence of soft electromagnetic interactions between the two colliding nuclei (also known as electromagnetic dissociation or EMD) can lead to breakup of the photon-emitting nucleus [32]. To facilitate the comparison with UPCs data, therefore, one has to account for the probability that a genuine photonuclear event, in which the photon-emitting nucleus is initially left unbroken (0nXn), could be rejected as a consequence of the presence of soft-electromagnetic interactions that lead to the dissociation of the photon-emitting nucleus. Under the hypothesis that the soft-excitation probability factorizes from the hard interaction [55], the no-breakup (survival) probability can be folded in the calculation of the effective photon flux. For this study, we considered the calculation of the photon flux in the presence of EM dissociation calculated in [52,56]. The validity of this theoretical approach, and its ability to accurately capture the impact of EMD in ultraperipheral collisions, has been demonstrated in a recent measurement of jet photoproduction in Pb-Pb collisions at the LHC. In that analysis, the no-breakup probability as a function of the momentum fraction carried by the partons in the emitted photon, as measured by ATLAS, is well described by a calculation based on the same theoretical framework adopted here. Within this approach, the photon flux in the presence of EMD is modeled as

$$f^{\text{eff}}_{\gamma/A}(z) = \int d^2\mathbf{b} P_{\text{no-EM}}(\mathbf{b}) \tilde{f}_{\gamma/A}(z,\mathbf{b}) \theta(|\mathbf{b}| - b_{\min}), \quad (7)$$

where the factor $P_{\text{no-EM}}$ is the probability that the electromagnetic breakup occurs in terms of the vector $\mathbf{b}$. In the left panel of Fig. 5, the no-breakup probability computed as the ratio of the photon fluxes described in Eqs. (5) and (7), is shown as a function of the photon energy fraction z. For this study, we relied on the interpolated Chebyshev parametrizations described in [52]. As expected, the ratio between the two fluxes decreases significantly with increasing photon energy, reflecting the enhanced probability of EM dissociation in small impact-parameter UPCs.

In the right panel of the same figure, we present the ratio of the predicted double-differential cross section with EMD effects to the one obtained without this correction. The calculation uses EPPS21 nuclear PDFs, the BCFY fragmentation function (see next section), and a charm-quark mass of $m_c = 1.3$ GeV. The resulting no-break-up probability, which we will employ throughout this manuscript to rescale the D^0 double-differential cross sections in UPCs, ranges from 0.83 to 0.68 for D^0 mesons with $0 < p_T < 1$ GeV and from 0.71 to 0.45 for those with $11 < p_T < 12$ GeV.

E. Fragmentation functions for heavy quarks

The charm-meson production cross section is computed within the QCD factorization framework by combining the partonic charm-quark production cross section with the quark-to-hadron fragmentation function. The latter one is a nonperturbative function which needs to be parametrized. Fragmentation of the heavy quark differs from the light

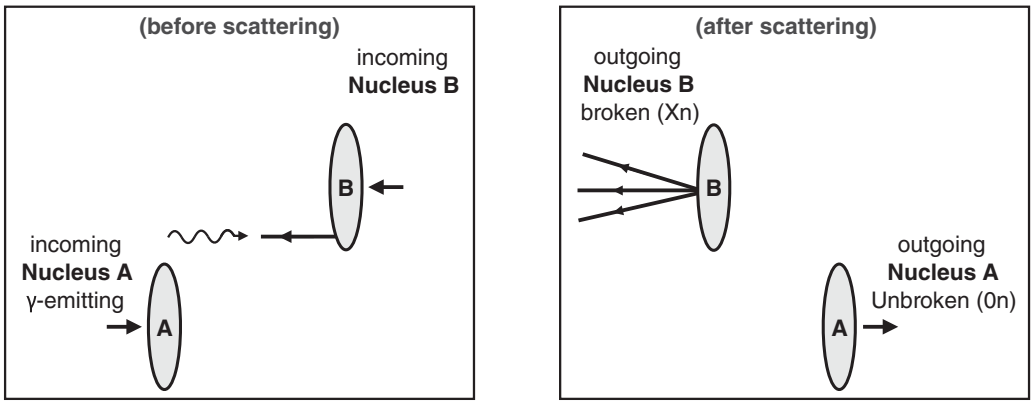

FIG. 4. Sketch of an ultraperipheral heavy-ion collision before (left) and after (right) the hard scattering.

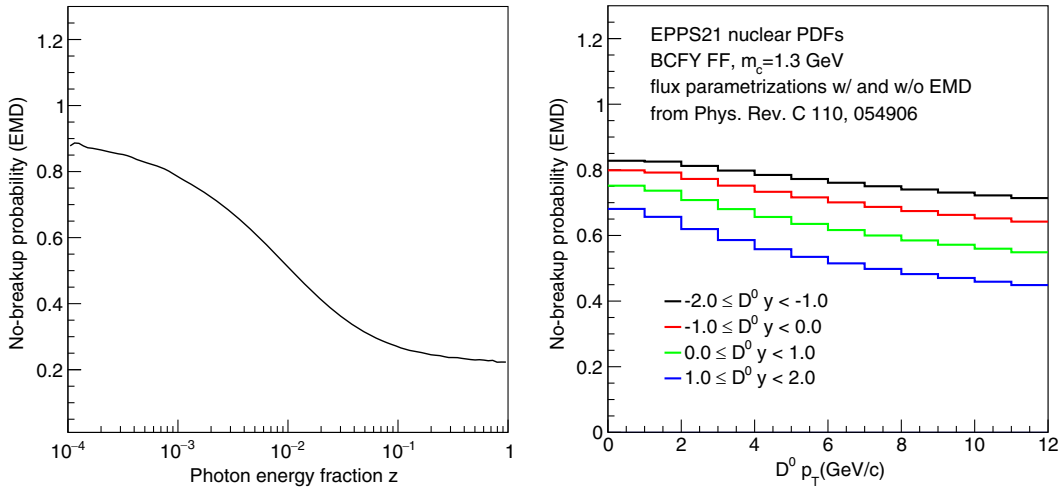

FIG. 5. Left: no-breakup probability (EMD) as a function of the photon energy fraction z. Right: no-breakup probability (EMD) as a function of the $D^0 p_T$, in different intervals of the D^0 y. The interpolated Chebyshev parametrizations of the photon fluxes used to compute these ratios are taken from [52].

quarks in that the heavy flavored meson should retain large fraction of the momentum of the original heavy quark. Therefore the fragmentation function for heavy quark should be peaked at large longitudinal momentum fraction z. One approach is to constrain such parametrization using the electron-positron data from LEP and then assume that they are universal and can be used for the other collision systems, including hadrons. Whether this procedure is applicable for hadronic collisions is still an open question, since the hadronization can be affected by the interactions with hadronic beam remnants, especially at low p_T and high rapidity. In the present analysis, we assess the impact of fragmentation by evaluating the cross section with two different parametrizations: the Peterson-Schlatter-Schmitt-Zerwas (PSSZ) [57] and Braaten-Cheung-Fleming-Yuan (BCFY) [58] fragmentation functions. To describe the HERA D^* photoproduction data, we employ the PSSZ fragmentation function [57]

$$D(z) = \mathcal{N}\frac{1}{z}\left(1-\frac{1}{z}-\frac{\varepsilon}{1-z}\right)^{-2}, \tag{8}$$

where $\mathcal{N}$ is a normalization constant. The parameter ε originally has the interpretation of being proportional to the ratio of squares of light to heavy quark masses, see [57]. In practice, however, it is commonly treated as a free parameter to obtain the best description of the data. We perform calculations with two choices of ε parameter: 0.02 and 0.035. These two values have been used in Ref. [39] for FONLL case and in Ref. [31] for fixed order NLO (FMNR calculation) respectively. The PSSZ function is normalized to unity, and then the fragmentation fraction is taken to include the fragmentation into the specific type of meson.

The Braaten-Cheung-Fleming-Yuan (BCFY) fragmentation function [58] was employed in Ref. [59] to model charm-meson production in hadronic collisions. In the latter study, the D^0 fragmentation function was constructed as a linear combination of two contributions: the component arising from D^* to D^0 decays and the so-called "primary" D^0 mesons produced directly in the hadronization of the charm quark. Schematically, one can write

$$F(c\to D^0) = F_p(c\to D^0) + F(c\to D^{*+})F(D^{*+}\to D^0) + F(c\to D^{*0})F(D^{*0}\to D^0). \tag{9}$$

The relation above contains contributions from the direct $c\to D^0$ hadronization and indirect $c\to D^*\to D^0$ channel. F_p is the fragmentation function for the primary D^0 production, $F(c\to D^{*+})$ and $F(c\to D^{*0})$ are fragmentation functions for production of D^* states, and functions $F(D^{*+}\to D^0)$ and $F(D^{*0}\to D^0)$ describe a decay of D^* states into D^0. The branching fractions for charm quarks fragmenting into D^0 and D^* are taken respectively [59]

$$\mathrm{BR}(c\to D^0_p) = 0.168, \qquad \mathrm{BR}(c\to D^*) = 0.235. \tag{10}$$

Taking into account that the branching fractions of D^{*0} and D^{*+} into D^0 meson are

$$\mathrm{BR}(D^{*0}\to D^0) = 1.0, \qquad \mathrm{BR}(D^{*+}\to D^0) = 0.677, \tag{11}$$

one can write Eq. (9) as (see [59])

$$D^{c\to D^0}(z,r) = 0.168 D^P(z,r) + 0.39\tilde{D}^V(z,r), \tag{12}$$

where

$$\tilde{D}^V(z,r) = \Theta\left(\frac{m_D}{m_{D^*}}-z\right)D^{(V)}\left(\frac{m_{D^*}}{m_D}z,r\right)\frac{m_{D^*}}{m_D}. \tag{13}$$

Functions $D^P(z,r)$ (for pseudoscalar state) and $\tilde{D}^V(z,r)$ (for vector state) are given explicitly in [58]. They depend on a single nonperturbative parameter r, which is the same for both functions. In the original model [58] this parameter can be interpreted as the ratio of the constituent mass of the light quark to the mass of the meson. Following [59,60], we take the value of parameter $r = 0.1$. For the case of D^* production the fragmentation function is

$$D^{c\to D^*}(z,r) = \mathrm{BR}(c \to D^*) D^V(z,r). \tag{14}$$

We also use this fragmentation function for the D^* production at HERA and compare the results with the ones obtained using PSSZ fragmentation function.

III. BENCHMARK WITH HERA DATA ON INCLUSIVE D^* PRODUCTION

Comprehensive study aimed on comparison of FONLL calculation with the HERA data on charm photoproduction [29,30] was performed in [39]. Later data from H1 [31] were also compared with several theoretical calculations. Among them was the fixed order NLO calculation in the massive scheme by Frixione-Mangano-Nason-Ridolfi (FMNR) [61,62] and the generalized-mass-variable-flavor-number-scheme (GMVFNS) calculation [63,64]. In the latter approach, which unifies fixed flavor massive scheme with zero-mass variable flavor scheme, large logarithmic corrections are resummed in universal parton distribution and fragmentation functions and finite mass terms were taken into account. It was found that both NLO calculations reproduced well the p_T and rapidity dependence of the experimental data from H1 experiment [31], within their uncertainties.

To ensure the consistency of calculation between HERA and UPC at LHC, we shall first revisit FONLL predictions [39] for HERA kinematics with more up-to-date proton PDFs which serve as proton benchmarks for the nuclear PDFs used for calculations at UPC LHC, and two different fragmentation functions. We use FONLL code [38,65] for calculations which provides both resummed (FONLL) and fixed order (FO) options. We perform the comparison with four sets of HERA data on D^* photoproduction [29–31]. In Table I we list the kinematic cuts on photon virtuality $Q^2_{\max}$, range for photon energy fraction of the electron energy $(z_{\min}, z_{\max})$, transverse momentum p_T and rapidity y or pseudorapidity η for these different datasets. Earlier data from H1 [29] and ZEUS [30] were taken at $E_e \times E_p = 27.5\ \mathrm{GeV} \times 820\ \mathrm{GeV}$, while 2012 data from H1 [31] were taken at $E_e \times E_p = 27.6\ \mathrm{GeV} \times 920\ \mathrm{GeV}$ energy combination. The two data samples from [29] labeled *ETAG33* and *ETAG44* were taken for two case when the electron is in the electron tagger at 33 m and 44 m, respectively. The average γp center-of-mass energy for the selected data was $\langle W \rangle = 194$ GeV for *ETAG33* and $\langle W \rangle = 83$ GeV for *ETAG44*.

For the photon PDF we tested two distributions AFG [66] and GRV [67], originally implemented in FONLL code. For the proton PDFs we used CT18ANLO [45], which is a proton baseline for nuclear PDF set EPPS21 [43]. We also compared it with calculations based on nNNPDF3.0p proton baseline set [44] and HERAPDF2.0 [48] set. Following [39] we used $\mu_F = \mu_R = \sqrt{p_T^2 + m_c^2} = \mu_0$ as a central choice of factorization and renormalization scale. We performed variation of factorization scale $\mu_F/\mu_0 = 0.5, 1.0, 2$ as well as variation of renormalization scale $\mu_R/\mu_0 = 0.5,\ 1.0,\ 2.0$, to obtain the uncertainty bands. We used charm mass $m_c = 1.3$ GeV, as this is the value used in CT18ANLO PDF set, but we also performed calculations with $m_c = 1.5$ GeV, the value for nNNPDF3.0 set. As discussed in previous section, we used PSSZ (8) and BCFY (14) fragmentation functions. In PSSZ function parameter was set to $\varepsilon = 0.02$ (used in [39] for FONLL calculation) and $\varepsilon = 0.035$ (used in FMNR calculation in [31]). For BCFY fragmentation function we used $r = 0.1$. The calculation is then multiplied by 0.47 which stems from the fragmentation fraction of $c \to D^*$ to be 23.5% and the fact that experiment measures $D^{*+} + D^{*-}$ contributions, see [39]. The presented cross sections are for electroproduction ($\sigma_{ep\to D^*X}$), therefore we multiplied the data by the factor coming from the photon flux from electron, integrated over given range of energies, (see discussion in [29,39]).

In Fig. 6 all four datasets from HERA are compared with the theoretical calculations based on the FONLL with PSSZ fragmentation function. The plots show transverse momentum distribution, while the rapidity (or pseudorapidity) is integrated out in the kinematic regions defined in Table I, corresponding to each dataset. The proton PDF used in all cases is CT18ANLO. The blue solid curve corresponds to FONLL and blue bands indicate the renormalization scale dependence while the factorization scale is fixed. There are also two cases shown, which indicate the factorization scale dependence (dotted and dashed magenta). As demonstrated in [39], and observed also here, the renormalization scale dependence is the dominant one, except for lower values of transverse momenta ($p_T \lesssim 2$ GeV) where factorization scale variation is sizeable. For some choices of renormalization and factorization scale the results become unreliable at low transverse momentum (see [39]). Thus for one of such scenario we only show the curve down to about 2 GeV. The charm quark mass is set to $m_c = 1.3$ GeV. The description of older H1 data is very good, for the ZEUS and later H1 data the FONLL prediction is somewhat too soft, the description is very good in the low p_T region and underestimates the data at higher p_T. Also the calculation based on newer PDFs is

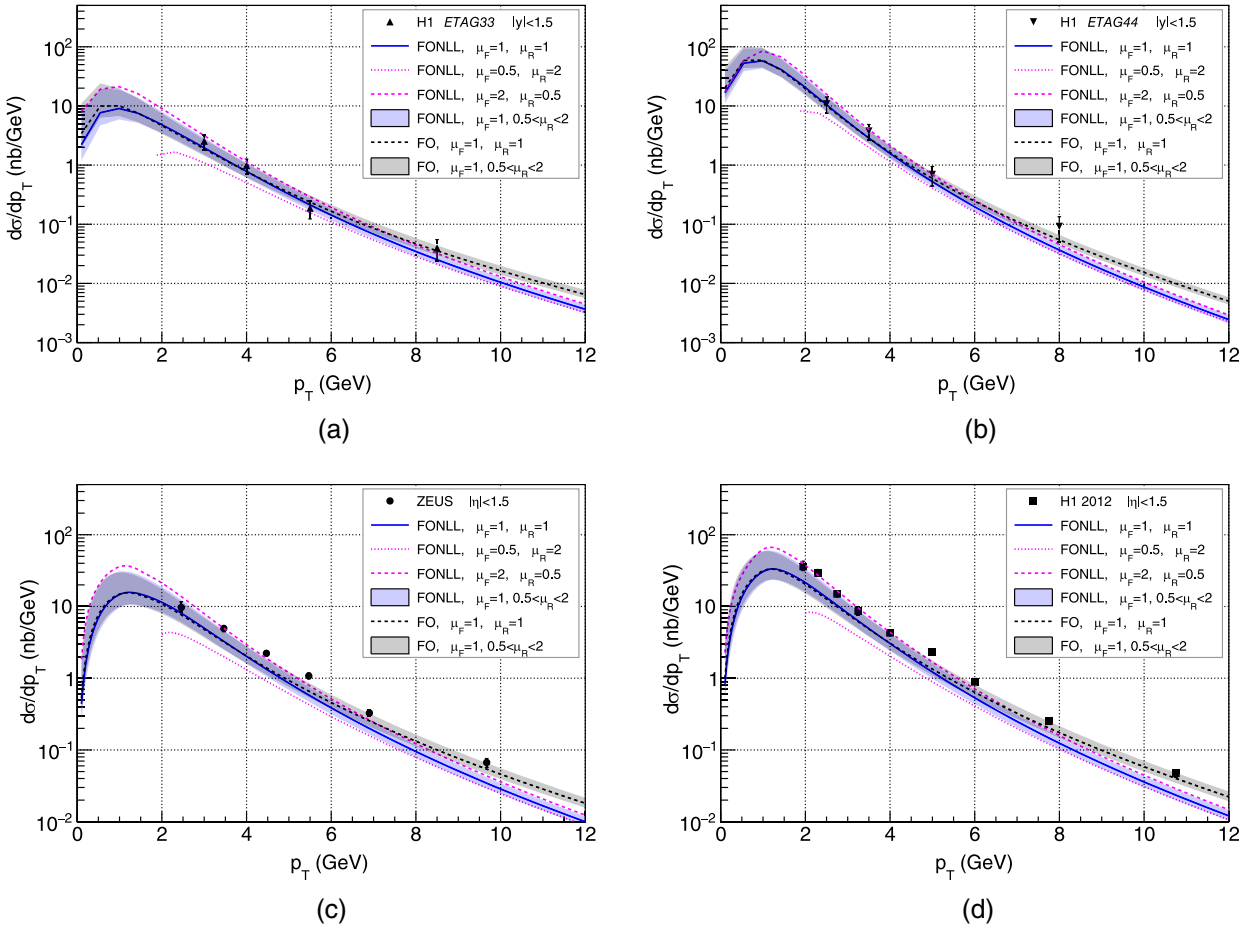

FIG. 6. Transverse momentum distribution D^* mesons in photoproduction in electron-proton collisions. FONLL calculation [39] $\mu_F = \mu_R = 1$ (blue solid). Shaded blue indicates variation of $0.5 < \mu_R < 2$ while $\mu_F = 1$ is fixed; magenta-dashed $\mu_F = 2.0, \mu_R = 0.5$, magenta-dotted $\mu_F = 0.5, \mu_R = 2.0$. FO calculation [39] $\mu_F = \mu_R = 1$ (black solid), and gray band corresponds to the variation of the renormalization scale. PSSZ fragmentation function is used with $\varepsilon = 0.02$ for FONLL and $\varepsilon = 0.035$ for FO. Compared with data from H1 [29] *ETAG33* (a) and *ETAG44* (b), ZEUS [30] (c) and H1 2012 [31] (d).

consistent with the original FONLL calculations [39] based on CTEQ5M PDF set[1] For comparison we also show the calculation based on the fixed order (FO) NLO calculation, black solid with gray bands. As mentioned above, for this calculation we take $\varepsilon = 0.035$, consistently with parameters used in FMNR calculation in [31]. The distribution is harder in that case, and the description of the data is slightly better, especially at higher p_T and this is particularly visible for ZEUS [30] and H1 2012 [31] data.

In Fig. 7 we compare the transverse-momentum distributions of D^0 mesons obtained with the PSSZ (blue band and curve) and BCFY (red band and curve) fragmentation functions. Relative to PSSZ, the BCFY parametrization yields a slightly harder p_T spectrum and provides a better description of the HERA data, particularly at high p_T.

In Figs. 8–10, we show FONLL rapidity and pseudorapidity distributions for various p_T cuts across multiple datasets. The rapidity convention matches that of HERA, with the proton beam taken as the positive direction. The blue bands represent the renormalization-scale uncertainty for the calculation employing the PSSZ fragmentation function, whereas the red bands correspond to the computation using BCFY. The solid blue and dashed red curves denote the respective central predictions. The factorization scale is fixed at $\mu_F/\mu_0 = 1$. Overall, the shape of the distributions are very well reproduced by both calculations. The calculation with BFCY fragmentation seems to be closer in normalization to data in majority of p_T bins.

Detailed comparison between FONLL-based calculations and predictions obtained using fixed-order calculations are shown in Appendix A.

We also studied the impact of changes in the photon and proton PDFs on the calculation. We checked that using AFG photon PDF [66] has negligible impact on the cross sections in the HERA kinematics. Similarly, we have

[1]For consistency check, we also used CTEQ5M PDF set in FONLL code and reproduced the calculations of [39].

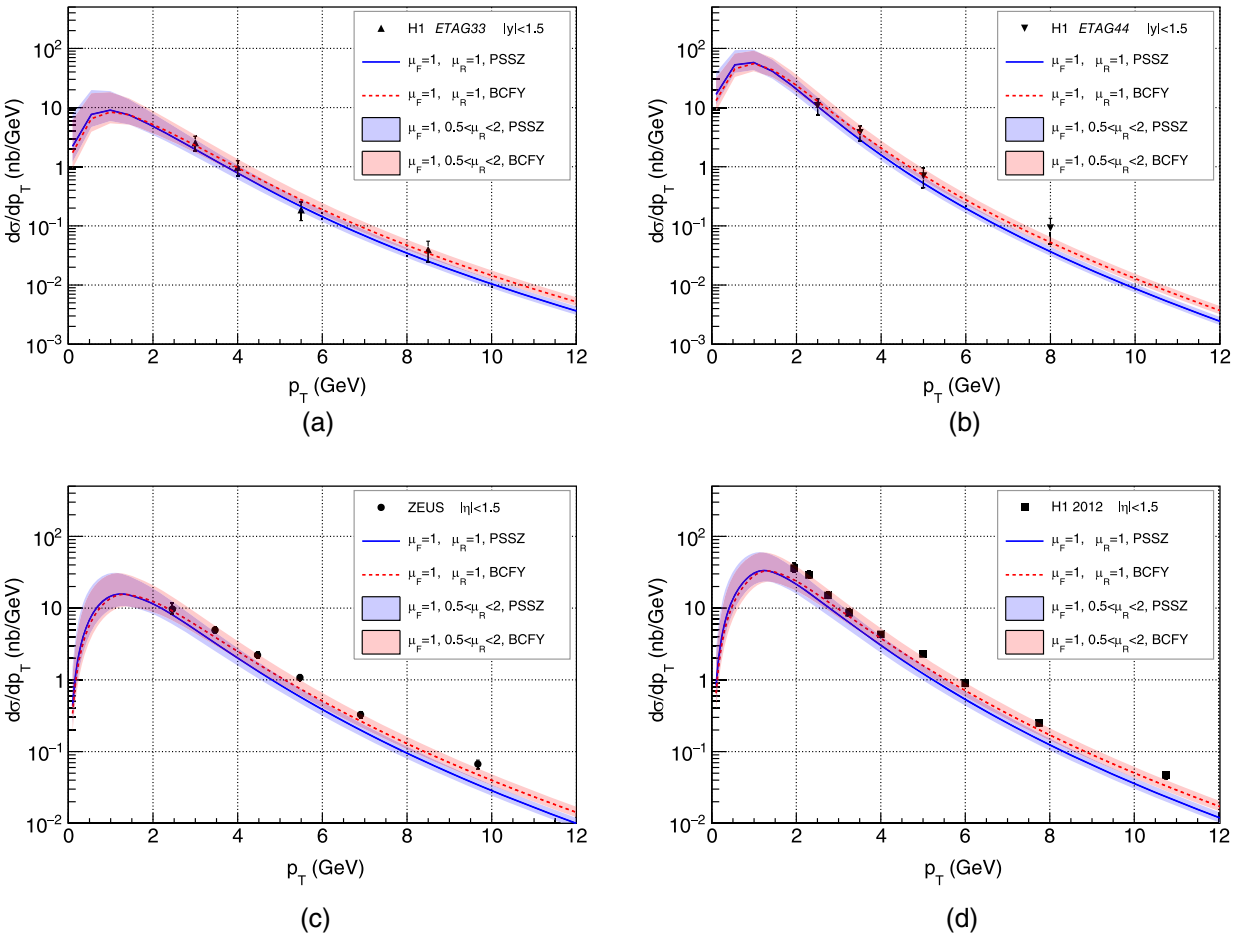

FIG. 7. Transverse momentum distribution D^* mesons in photoproduction in electron-proton collisions obtained from FONLL [39]. Bands indicate the variation of $0.5 < \mu_R < 2$ while $\mu_F = 1$ is fixed. Blue band: PSSZ fragmentation function with $\varepsilon = 0.02$, red band: BCFY fragmentation function with $r = 0.1$. Compared with data from H1 [29] *ETAG33* (a) and *ETAG44* (b), ZEUS [30] (c) and H1 2012 [31] (d).

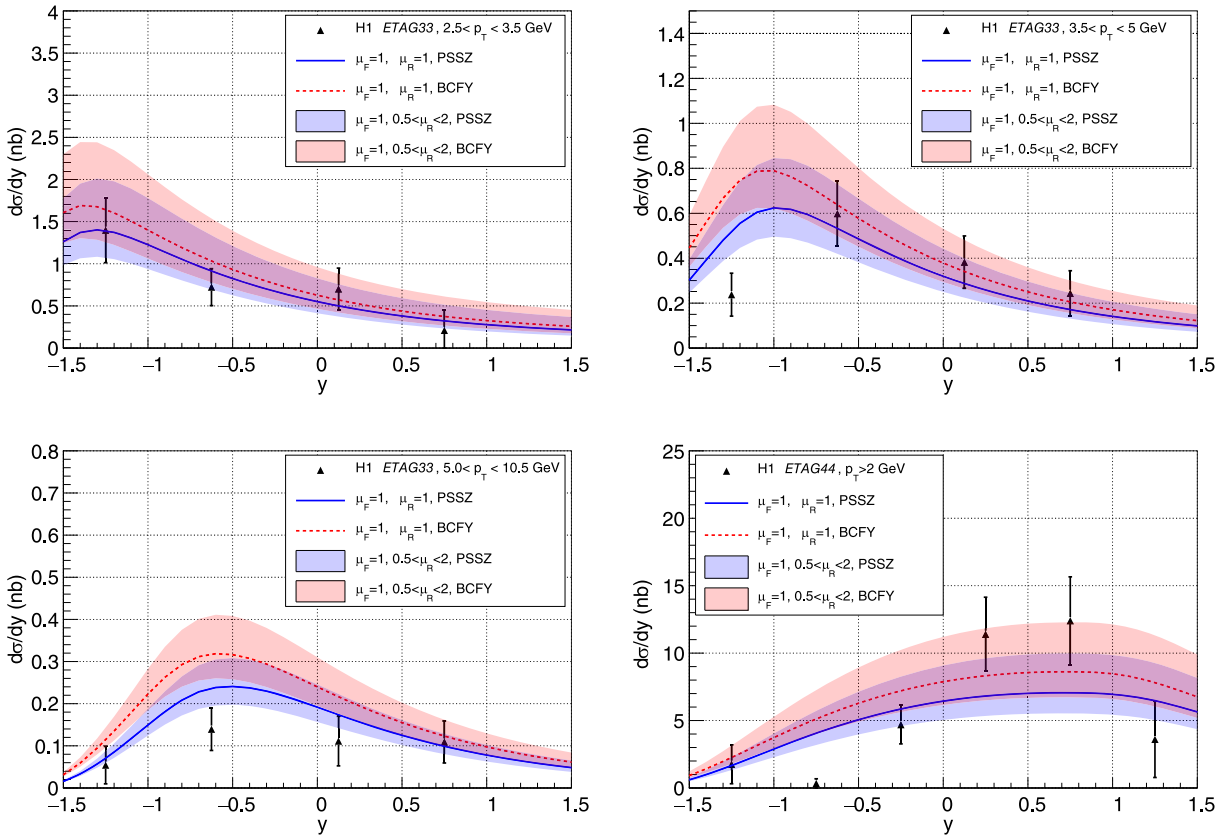

FIG. 8. Rapidity distribution of D^* mesons in photoproduction in electron-proton collisions at HERA from FONLL calculation [39]. Bands denote renormalization scale variation $0.5 < \mu_R < 2$ while $\mu_F = 1$ is fixed. Blue band: PSSZ fragmentation function with $\varepsilon = 0.02$, red band BCFY fragmentation function with $r = 0.1$. Compared with data from H1 [29], for different p_T bins. Note different vertical scales. Positive rapidity is proton going direction.

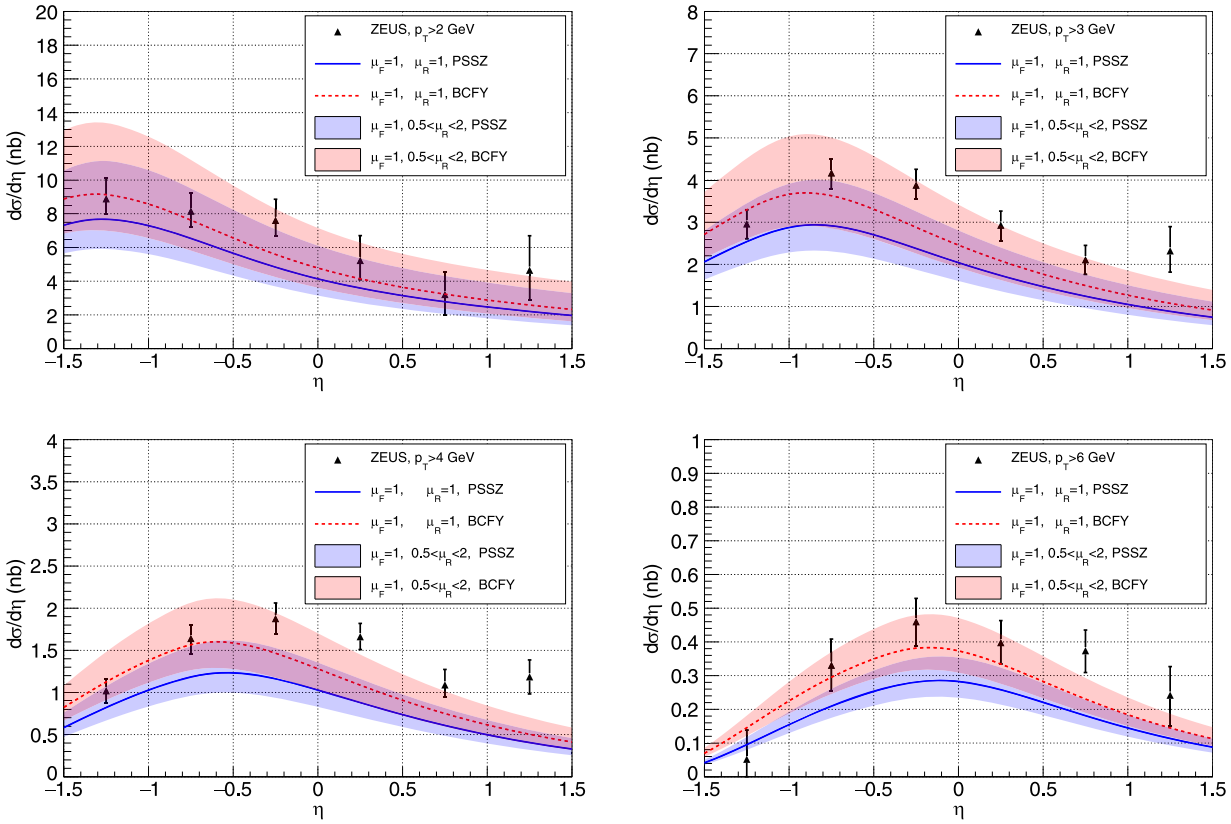

FIG. 9. Pseudorapidity distribution of D^* mesons in photoproduction in electron-proton collisions at HERA from FONLL calculation [39]. Bands denote renormalization scale variation $0.5 < \mu_R < 2$ while $\mu_F = 1$ is fixed. Blue band: PSSZ fragmentation function with $\varepsilon = 0.02$, red band BCFY fragmentation function with $r = 0.1$. Compared with data from ZEUS [30], for different minimum p_T cuts: 2,3,4,6 GeV. Note different vertical scales. Positive pseudorapidity is proton direction.

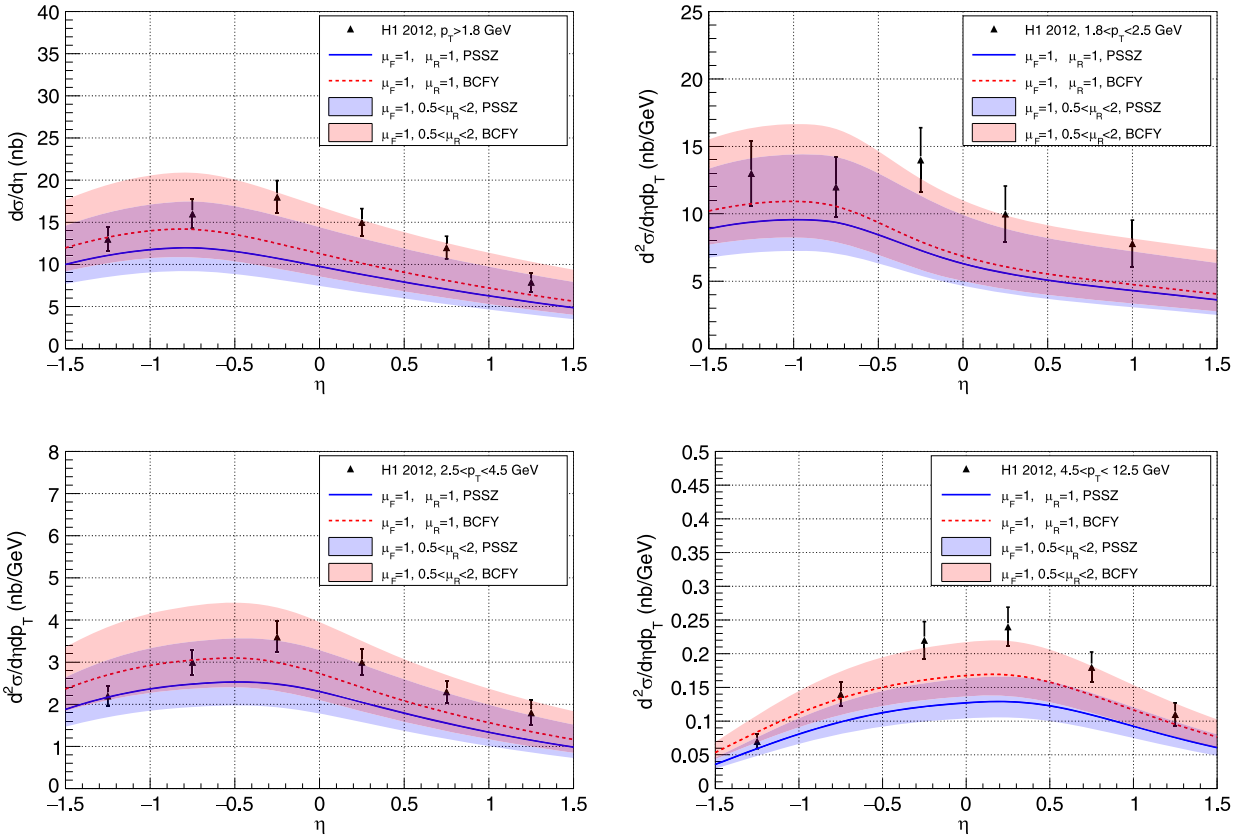

FIG. 10. Pseudorapidity distribution of D^* mesons in photoproduction in electron-proton collisions at HERA from FONLL calculation [39]. Bands denote renormalization scale variation $0.5 < \mu_R < 2$ while $\mu_F = 1$ is fixed. Blue band: PSSZ fragmentation function with $\varepsilon = 0.02$, red band BCFY fragmentation function with $r = 0.1$. Compared with data from H1 [31], for different p_T bins. Note that data and results in three p_T bins (1.8,2.5), (2.5,4.5), (4.5,12.5) are presented as double differential cross sections. Positive pseudorapidity is proton direction.

checked that the differences between the calculations using CT18ANLO, HERAPDF2.0 and nNNPDF3.0_p are of the order of few percent for $p_T > 2$ GeV, and only in the very low p_T region (< 1 GeV) the differences become larger. We have also tested the sensitivity of the calculation to the different value of charm mass. Increasing mass of the heavy quark leads to the harder p_T spectrum. At low values of p_T the calculation with higher mass is suppressed, while at higher values of p_T it is enhanced since the effect of the logarithmic resummation is smaller for this case (see discussion in [39]).

Summarizing, we have updated FONLL calculations with newer proton PDFs and compared with the HERA data on D^* photoproduction. The change due to the proton PDF is small with respect to the original calculations presented in [39]. Overall the data are well described by the FONLL calculation with BCFY fragmentation function. The calculation with PSSZ fragmentation function describes older H1 [29] data reasonably well, while it leads to softer p_T spectrum than the ZEUS [30] and H1 data from 2012 [48]. The calculation with BCFY fragmentation function leads to a better description of the HERA data, especially at high values of transverse momenta.

IV. PREDICTIONS FOR D^0 PRODUCTION IN PbPb ULTRAPERIPHERAL COLLISIONS AT THE LHC

Having validated the FONLL calculations against the D^* photoproduction data at HERA, we now address the calculations of the D^0 inclusive production in ultraperipheral collisions at the LHC. Since the nucleus, which is the source of the photons, is not detected, one should in principle integrate the flux over the entire range of photon energies. In practice, we assume that the fractional energy of the photon is limited by

$$z \in [z_{\min}, z_{\max}]. \tag{15}$$

We take $z_{\max} = 0.1$ based on the fact that the photon flux from the nucleus is negligible beyond there, as evident from Fig. 3. The minimal value $z_{\min}$ is given by

$$z_{\min} = \frac{M^2_{c\bar{c}}}{s}, \tag{16}$$

where the invariant mass of the charm pair is $M^2_{c\bar{c}} = 2m_T^2(1 + \cosh(y_1 - y_2))$. In practice we take the lower

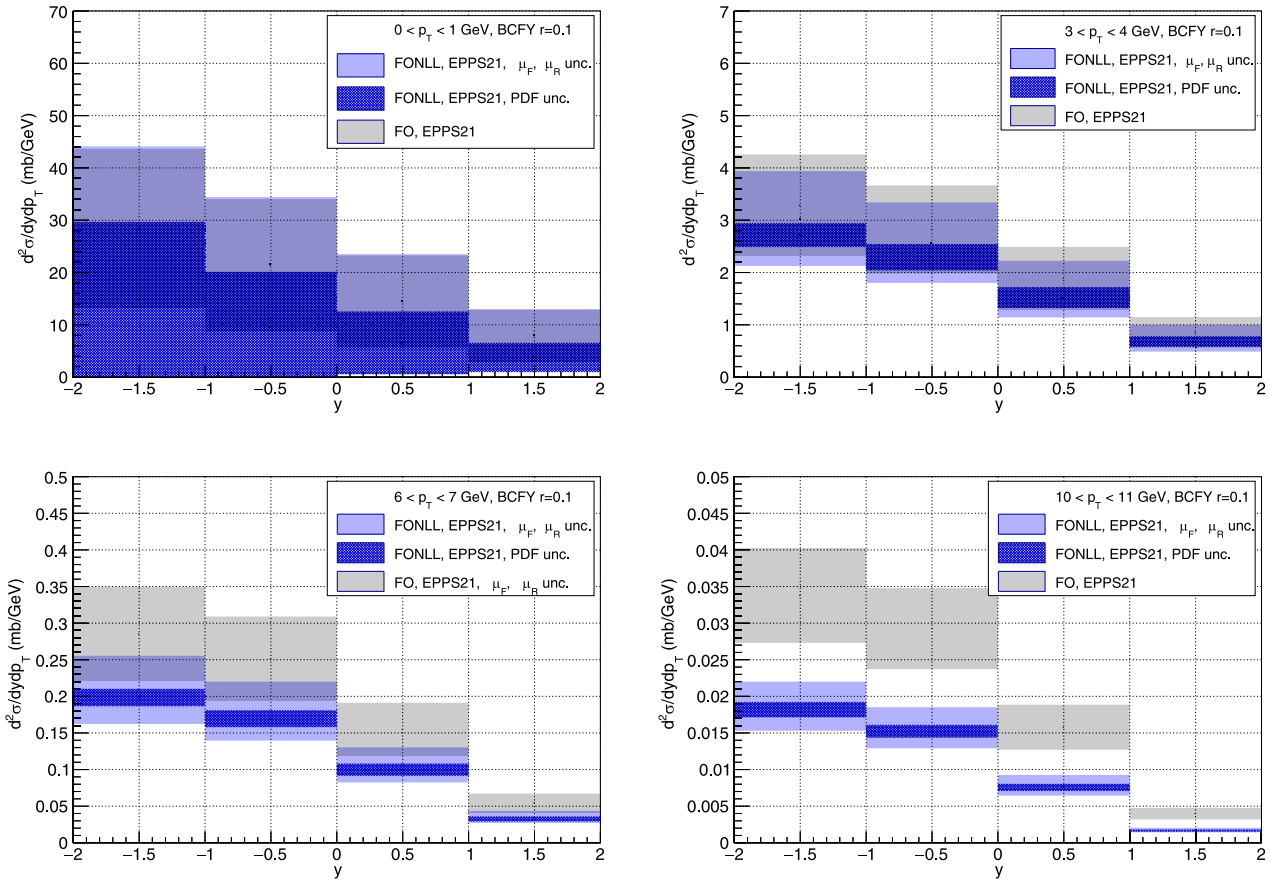

FIG. 11. Rapidity distribution for the D^0 production in UPC PbPb collisions at $\sqrt{s_{\rm NN}} = 5.36$ TeV. Four panels correspond to p_T bins (0–1), (3–4), (6–7), (10–11) GeV. Light blue band: FONLL calculation with factorization and renormalization scale variation, gray band: FO calculation with factorization and renormalization scale variation, dark blue band: FONLL EPPS21 [43] PDF uncertainty. Both FONLL and FO calculation done with BCFY fragmentation function [58,59] with parameter $r = 0.1$. Photon-emitting nucleus is moving in the positive rapidity direction.

limit $z_{\rm min} = \frac{4m_c^2}{s}$ (we checked that moving the cutoff to $z_{\rm min} = 10^{-5}$ does not affect the calculation within the rapidity range of $[-2, 2]$).

As discussed in Sec. II B, for the nuclear PDF we used the EPPS21 [43] set as well as the nNNPDF3.0 [44] set. In addition, we also perform the calculations with the EPPS21 proton baseline PDF CT18ANLO [45]. This allows to quantify the size of the nuclear effects in the kinematics for D^0 production at CMS.

For the fragmentation, we adopt the BCFY parametrization, as described in Eq. (12), with $r = 0.1$ [58]. For comparison we also used PSSZ function with $\varepsilon = 0.2$ and $\varepsilon = 0.035$ [57]. Finally, the results have been corrected by the EMD factor, described in Sec. II D 2 and shown in the right plot of Fig. 5, to account for the survival probability of the nucleus due to the photon interactions.

We first present the results of theoretical calculations in the finer bins in p_T, studying the sensitivity due to the variation of different parameters. In the following section we show the comparison of calculations in the bins used by CMS in their measurement [32].

In Fig. 11 distributions in rapidity for D^0 production are shown as a function of p_T and rapidity in four bins of p_T: (0–1), (3–4), (6–7), (10–11) GeV and rapidity range $-2 < y < 2$. The convention in these plots is such that the positive rapidity is the photon going direction, thus it is reverse with respect to HERA. FONLL calculation is shown (blue band) for the BCFY choice of the fragmentation function with parameter $r = 0.1$, and EPPS21 nPDF is used. The bands correspond to the variation of the factorization $\mu_F/\mu_0 = 0.5$, 1.0, 2.0 and renormalization scales $\mu_R/\mu_0 = 0.5$, 1.0, 2.0, (with constraint $1/2 \leq \mu_F/\mu_R \leq 2$) where $\mu_0 = \sqrt{p_T^2 + m_c^2}$ and charm mass was set to $m_c = 1.3$ GeV (consistent with the charm mass value used in the EPPS21 PDF set). The inner, dark blue band in FONLL calculation is the EPPS21 PDF uncertainty. We see that, for moderate and high p_T, the PDF uncertainty is much smaller than the variation of the renormalization and factorization scales. It is in the lowest p_T bin, that the nPDF uncertainty is quite large and comparable to the scale uncertainty. It is understood, since the PDF uncertainty will also directly influence

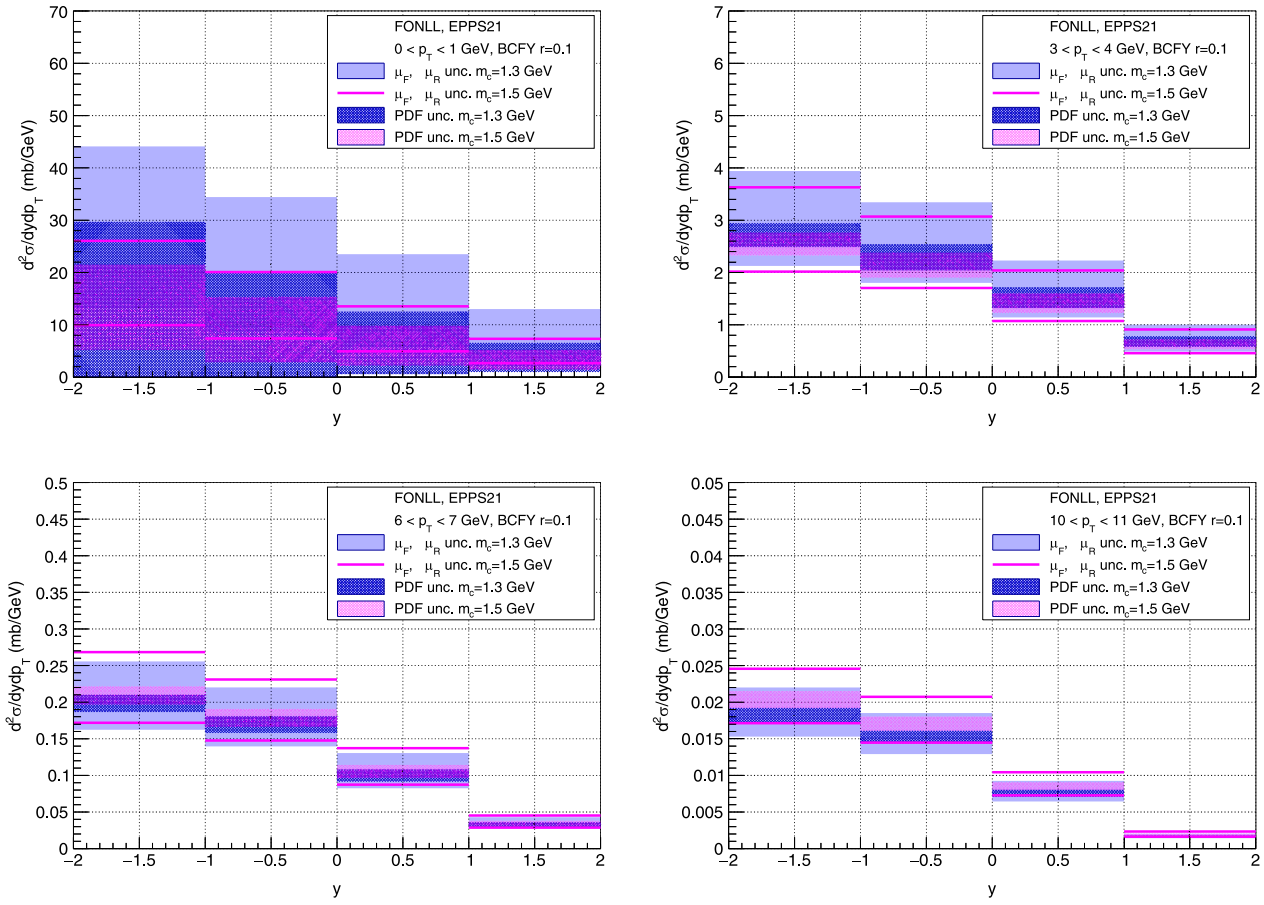

FIG. 12. Rapidity distribution for the D^0 production in UPC PbPb collisions at $\sqrt{s_{\mathrm{NN}}} = 5.36$ TeV with EPPS21 nuclear PDF. Four panels correspond to p_T bins (0–1), (3–4), (6–7), (10–11) GeV. Light blue band: FONLL calculation with factorization and renormalization scale variation for $m_c = 1.3$ GeV, magenta lines band: FONLL calculation with factorization and renormalization scale variation and $m_c = 1.5$ GeV, dark blue band: FONLL EPPS21 [43] PDF uncertainty, $m_c = 1.3$ GeV. Magenta band: FONLL EPPS21 [43] PDF uncertainty, $m_c = 1.5$ GeV. BCFY fragmentation function [58,59] with parameter $r = 0.1$. Photon-emitting nucleus is moving in the positive rapidity direction.

the magnitude of the scale uncertainty. For comparison we also show FO calculation (gray bands) in Fig. 11. As observed for the HERA case, the FO is higher than FONLL at large p_T.

In Fig. 12 the FONLL results are plotted, but using two different mass choices for the charm quark $m_c = 1.3$ and $m_c = 1.5$ GeV for the EPPS21 nuclear PDF. Similar to the case of the HERA data, the higher value of the charm mass leads to slightly lower results for low p_T but higher values for highest p_T bins. The high p_T trend is related to the FONLL resummation. The scale and PDF uncertainties are slightly smaller for $m_c = 1.5$ GeV.

In Fig. 13 a similar study on the charm mass dependence is shown, but the nuclear PDF is taken to be equal to A (mass number) times the proton PDF. For the proton PDF CT18ANLO is selected. Therefore this calculation is without any effects of nuclear modification. We observe that the calculations are comparable to the ones with nuclear PDFs for two higher p_T bins. For the lowest p_T bin the theoretical calculations are slightly higher than for EPPS21 case, as expected due to the increased role of the shadowing at small x and p_T. More precisely, at the largest values of rapidity, which corresponds to smallest values of x, the nuclear shadowing leads to a reduction of cross section at the level of about 30%–40% at $p_T < 2$ GeV, 15%–20% at $3 < p_T < 7$ GeV, and less than 10% for $p_T > 9$ GeV.

In Fig. 14 the same distributions in rapidity are shown for FONLL and FO but for the case of the AFG photon PDF [66], with just variation in renormalization and factorization scale, using nuclear EPPS21 PDF set. Comparing with Fig. 11 we see that the differences between GRV and AFG photon PDFs are completely negligible in the kinematics studied.

In Fig. 15 the same distributions in rapidity are shown but for different choices of the fragmentation function (nuclear PDF is still EPPS21). Here we show the FONLL with PSSZ function and parameter $\varepsilon = 0.02$ and FO

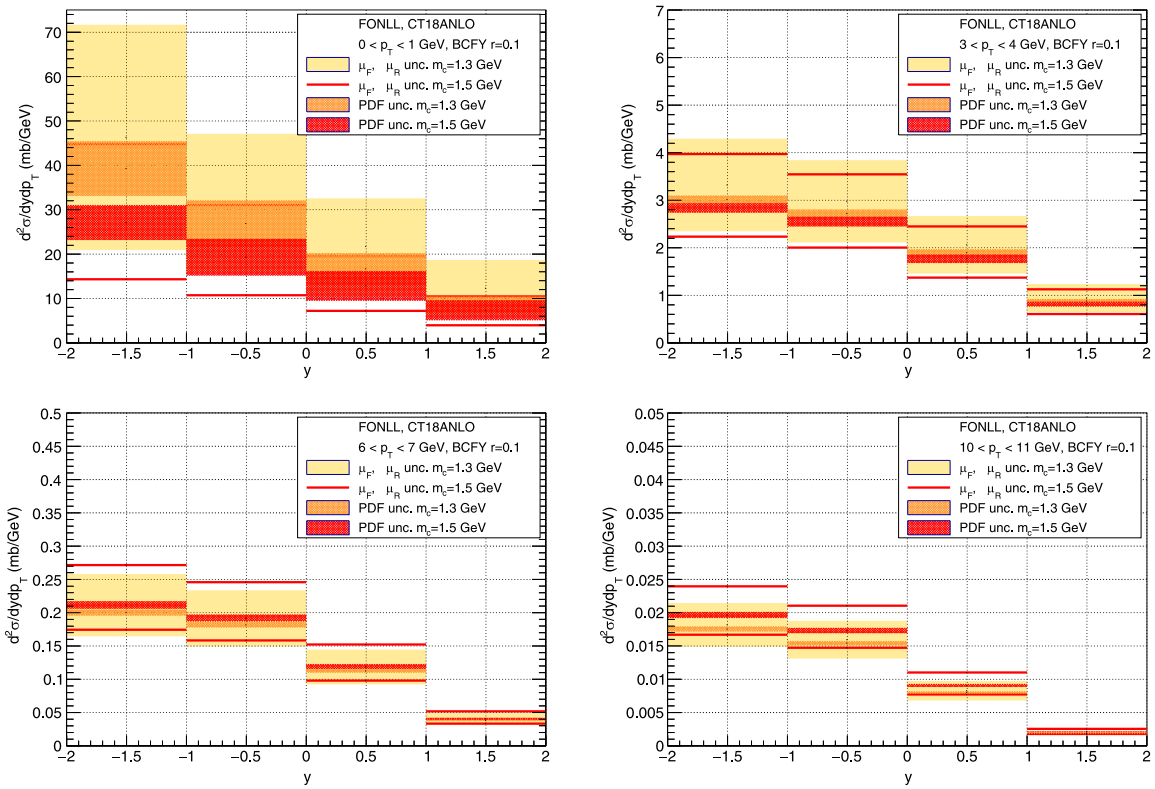

FIG. 13. Rapidity distribution for the D^0 production in UPC PbPb collisions at $\sqrt{s_{NN}} = 5.36$ TeV with CT18ANLO proton PDF. Four panels correspond to p_T bins (0–1), (3–4), (6–7), (10–11) GeV. Yellow band: FONLL calculation with factorization and renormalization scale variation for $m_c = 1.3$ GeV, red lines band: FONLL calculation with factorization and renormalization scale variation and $m_c = 1.5$ GeV, orange band: FONLL CT18ANLO [43] PDF uncertainty, $m_c = 1.3$ GeV. Red band: FONLL CT18ANLO [43] PDF uncertainty, $m_c = 1.5$ GeV. BCFY fragmentation function [58,59] with parameter $r = 0.1$. Photon-emitting nucleus is moving in the positive rapidity direction.

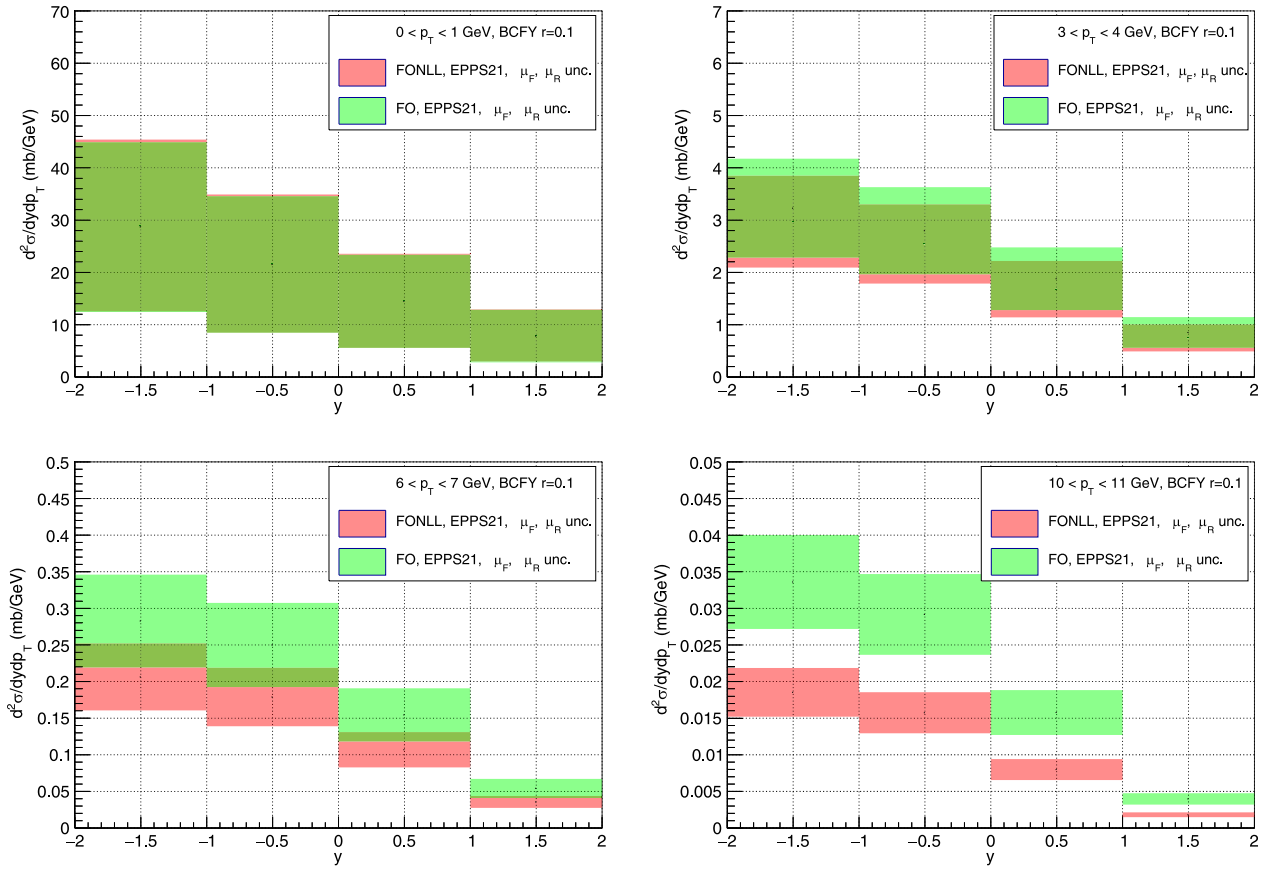

FIG. 14. Rapidity distribution for the D^0 production in UPC PbPb collisions at $\sqrt{s_{NN}} = 5.36$ TeV. Calculations with AFG photon PDF. Four panels correspond to p_T bins (0–1), (3–4), (6–7), (10–11) GeV. Red band: FONLL calculation with factorization and renormalization scale variation, green band: FO calculation with factorization and renormalization scale variation. FONLL and FO calculation done with BCFY fragmentation function with parameter $r = 0.1$. Photon-emitting nucleus is moving in the positive rapidity direction.

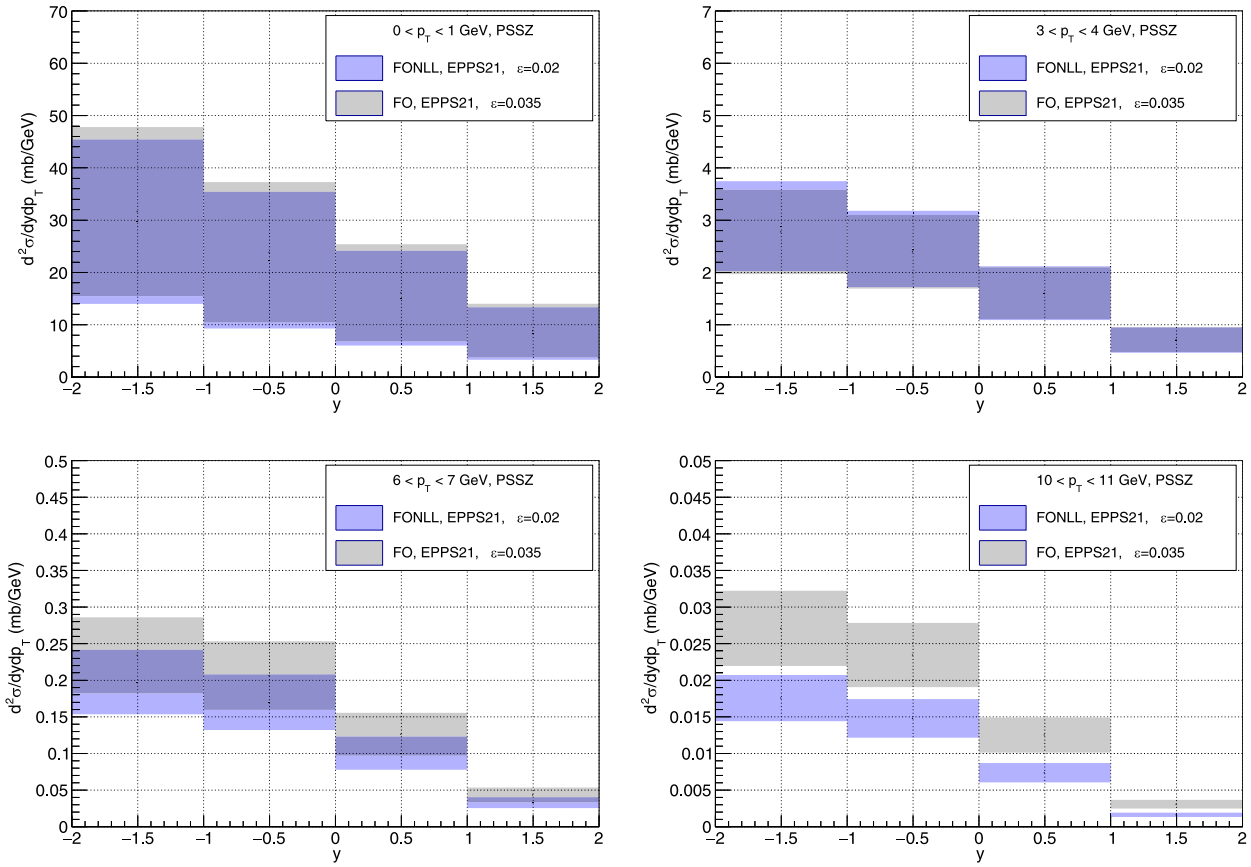

FIG. 15. Rapidity distribution for the D^0 production in UPC PbPb collisions at $\sqrt{s_{NN}} = 5.36$ TeV. Four panels correspond to p_T bins (0–1), (3–4), (6–7), (10–11) GeV. Light blue band: FONLL calculation with factorization and renormalization scale variation, gray band: FO calculation with factorization and renormalization scale variation. FONLL and FO calculation done with PSSZ fragmentation function with parameter $\varepsilon = 0.02$ and 0.035 respectively. Photon-emitting nucleus is moving in the positive rapidity direction.

calculation with PSSZ function and parameter $\varepsilon = 0.035$. This is the same setup as presented in Fig. 6 for the HERA data. We see that the FONLL and FO are somewhat closer for the highest p_T bin, than in the case of the BCFY fragmentation function. This is understandable, since the fragmentation with $\varepsilon = 0.035$ leads to a softer spectrum than with $\varepsilon = 0.02$. Overall, the differences between the two fragmentation schemes BCFY and PSSZ are very small in the studied range of p_T and y, with BCFY fragmentation function resulting in slightly higher cross section at large values of p_T as was found for ep case in Sec. III.

For the sake of completeness, and despite the two separate contributions being unphysical (e.g., [38,64]) and dependent on what theoretical approach and parameters are used, we have also explored the relative sizes of the direct and resolved cross sections. Within the approach that we have chosen (FONLL, with a massive NLO calculation matched to a massless NLL-resummed one, with the introduction of a damping function $G(m, p_T)$ (see Eq. (1), with its free parameter c set to 5, for suppressing spurious higher orders terms), we observe that the direct contribution tends to dominate at positive rapidities and medium transverse momentum values ($p_T < 10$ GeV), whereas the resolved contribution can reach up to about 50% in two kinematical regions, namely a small region of negative rapidities ($y < 1$) and small transverse momentum ($p_T < 1$ GeV), and a broader region of transverse momentum larger than about 10 GeV.

Appendix B presents supplementary plots of the calculations versus transverse momentum, binned in rapidity, for the EPPS21, nNNPDF3.0, and CT18ANLO PDF sets.

V. COMPARISON WITH CMS MEASUREMENT

In this section, the GγA-FONLL predictions are compared to the first measurement of photonuclear D^0 meson production in ultraperipheral heavy-ion collisions, recently performed by the CMS Collaboration at the LHC [32]. The measurement uses 1.38 nb^{-1} of lead-lead data collected at $\sqrt{s_{NN}} = 5.36$ TeV. Photonuclear events were selected by requiring that at least one of the two colliding nuclei breaks (0nXn), using the zero degree calorimeters, and by imposing the presence of a large rapidity gap in the direction of the photon-emitting nucleus. The measurement

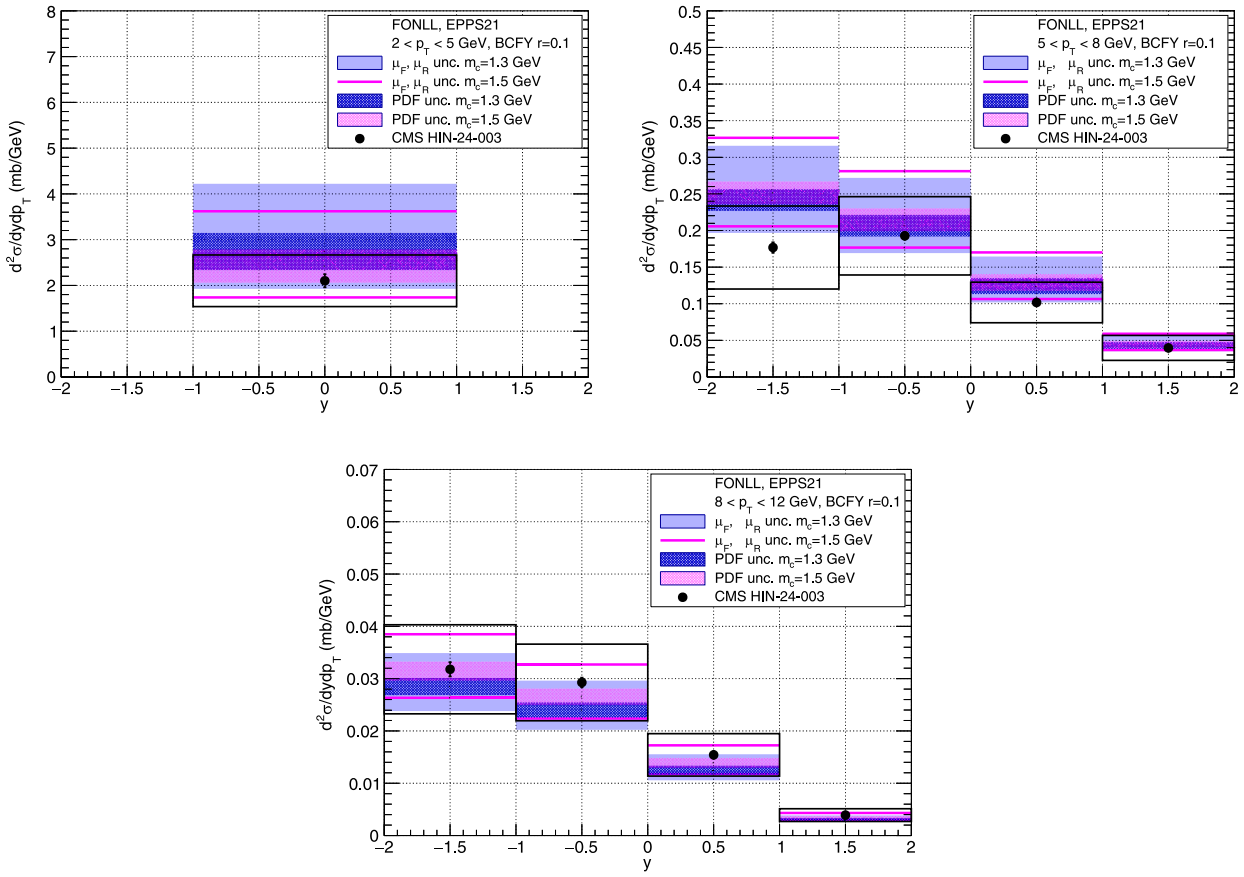

FIG. 16. Rapidity distribution for the D^0 production in UPC PbPb collisions at $\sqrt{s_{\mathrm{NN}}} = 5.36$ TeV with EPPS21 nuclear PDF in p_T bins (2–5), (5–8), (8–12) GeV. Light blue band: FONLL calculation with factorization and renormalization scale variation for $m_c = 1.3$ GeV, magenta lines band: FONLL calculation with factorization and renormalization scale variation and $m_c = 1.5$ GeV, dark blue band: FONLL EPPS21 [43] PDF uncertainty, $m_c = 1.3$ GeV. Magenta band: FONLL EPPS21 [43] PDF uncertainty, $m_c = 1.5$ GeV. BCFY fragmentation function [58,59] with parameter $r = 0.1$. Data are from CMS [32].

was performed as a function of the transverse momentum and rapidity of the D^0 meson, in the ranges $2 < p_T < 12$ GeV and $-2 < y < 2$. Specifically, the $2 < p_T < 5$ GeV interval was measured in one rapidity bin, $|y| < 1$, while the $5 < p_T < 8$ GeV and $8 < p_T < 12$ GeV intervals were measured in four equal-size rapidity bins spanning $-2 < y < 2$.

In Fig. 16, the GγA-FONLL predictions obtained with EPPS21 nuclear PDFs are compared to the CMS data. Two calculations are shown: one with $m_c = 1.3$ GeV, which is the charm quark mass used in the extraction of the EPPS21 set, and another with $m_c = 1.5$ GeV to test the sensitivity of the prediction to the charm mass. Figure 17 shows analogous predictions obtained using the nNNPDF3.0 set ($m_c = 1.5$ GeV).

Within the still sizeable experimental uncertainties, the data are well described by the GγA-FONLL predictions obtained using both EPPS21 and nNNPDF3.0 across all p_T and rapidity bins. The central values of the data appear to favor calculations with a larger charm quark mass.

In Fig. 18, the experimental data are compared to the GγA-FONLL predictions obtained using the CT18ANLO proton PDF for two values of the charm quark mass, $m_c = 1.3$ and 1.5 GeV. In the two lower p_T intervals of Fig. 18, the calculations using proton PDFs systematically overshoot the data. The nuclear modifications in the $2 < p_T < 5$ GeV interval amount to approximately 20%, while in the intermediate $5 < p_T < 8$ GeV range they lie between 5% and 15%, with stronger suppression observed at higher rapidities. The comparison with predictions using proton PDFs suggests that the absence of nuclear modifications significantly reduces the agreement with the experimental data. The need for sizable nuclear effects is particularly evident for low-p_T D^0 mesons at forward rapidity, where low-x effects play a more prominent role. This effect certainly deserves a further detailed analysis. We only tested here the parton densities obtained using standard linear Dokshitzer-Gribov-Lipatov-Altarelli-Parisi evolution but it is well known [68] that it is precisely the low p_T, low x regime where gluon recombination effects

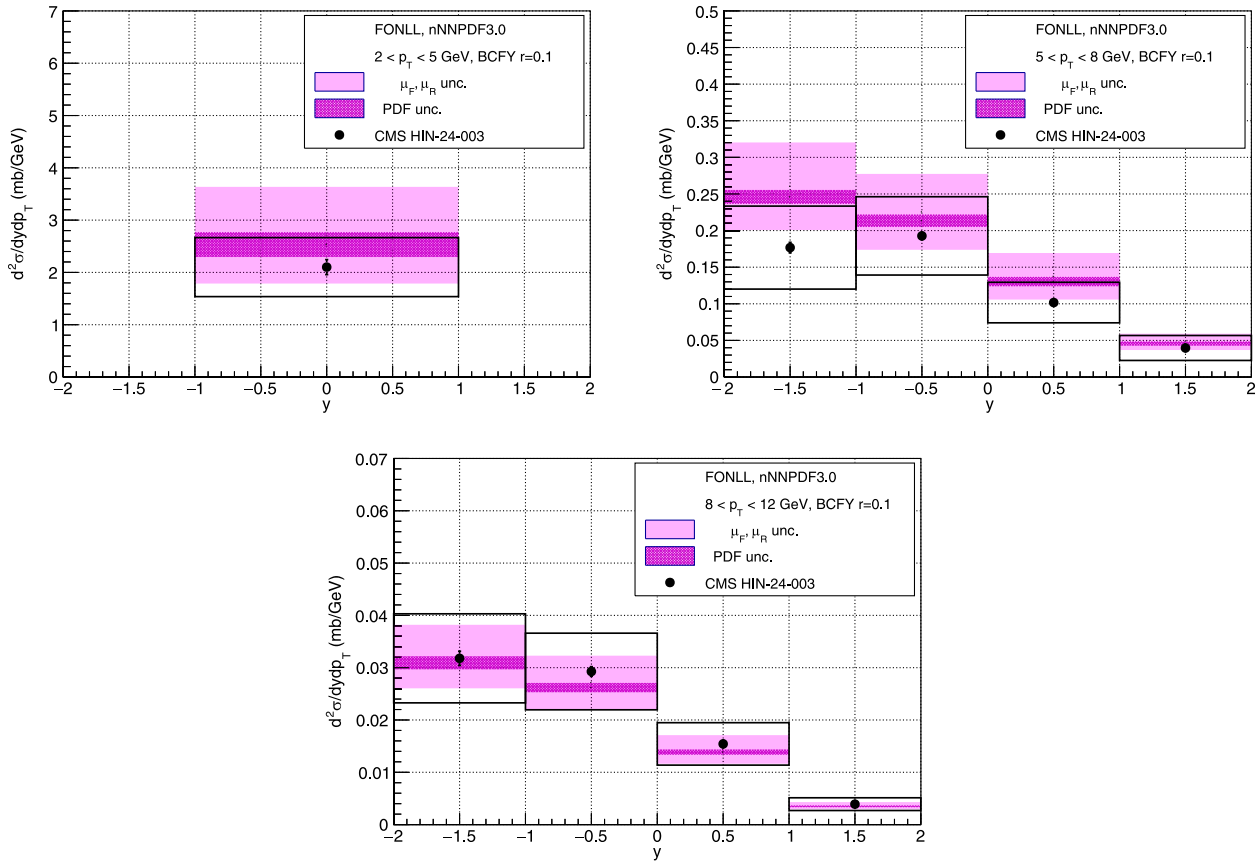

FIG. 17. Rapidity distribution for the D^0 production in UPC PbPb collisions at $\sqrt{s_{NN}} = 5.36$ TeV with nNNPDF3.0 nuclear PDF in p_T bins (2–5), (5–8), (8–12) GeV. Light magenta band: FONLL calculation with factorization and renormalization scale variation for $m_c = 1.3$ GeV, darker magenta band PDF uncertainty, $m_c = 1.5$ GeV. BCFY fragmentation function [58,59] with parameter $r = 0.1$. Data are from CMS [32].

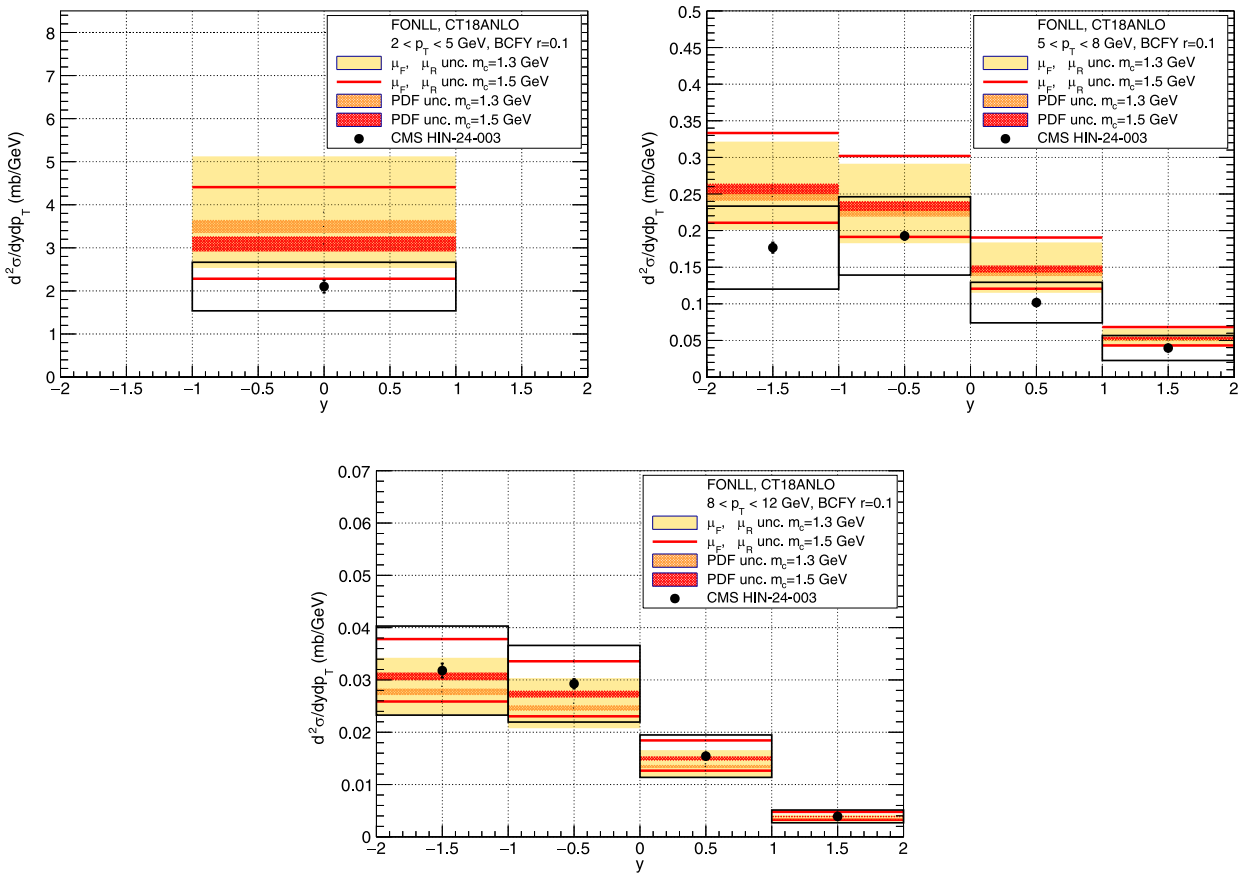

FIG. 18. Rapidity distribution for the D^0 production in UPC PbPb collisions at $\sqrt{s_{NN}} = 5.36$ TeV with CT18ANLO proton PDF in p_T bins (2–5), (5–8), (8–12) GeV. Yellow band: FONLL calculation with factorization and renormalization scale variation for $m_c = 1.3$ GeV, red lines band: FONLL calculation with factorization and renormalization scale variation and $m_c = 1.5$ GeV, orange band: FONLL CT18ANLO [43] PDF uncertainty, $m_c = 1.3$ GeV. Red band: FONLL CT18ANLO [43] PDF uncertainty, $m_c = 1.5$ GeV. BCFY fragmentation function [58,59] with parameter $r = 0.1$. Data are from CMS [32].

are expected to be important and can lead to saturation. They can be accounted for by including in the evolution the nonlinear terms in parton density. One can then potentially expect sizeable modifications to the cross section, as demonstrated in work on nuclear PDFs and nonlinear GLR-MQ equation [69]. The impact of nonlinear evolution for parton densities used in the charm photoproduction process, while being beyond the scope of the present work, certainly deserves to be investigated further, and we postpone it for the future study.

Finally, we note that in the highest p_T bin, where nuclear effects are expected to be negligible, the central FONLL predictions, obtained with both proton and nuclear PDFs, lie slightly below the data. Interestingly, a similar trend was observed at HERA, where the FONLL prediction yielded a slightly softer p_T spectrum than the experimental data (see Sec. III).

VI. CONCLUSIONS

In this paper we presented calculations of charm photoproduction in electron-proton collisions at HERA and in ultraperipheral heavy-ion collisions (UPCs) at the LHC with the new GγA-FONLL framework.

We performed detailed comparison with HERA measurements of D^* production in electron-proton collisions, employing resummed FONLL calculations as functions of the D^* transverse momentum and rapidity. We examined how the predictions vary with different photon and proton PDF parametrizations and assessed the impact of alternative fragmentation functions. The calculations agree with earlier FONLL predictions and with the ep measurements at HERA. As previously observed in earlier FONLL studies, the predictions tend to be marginally softer than the measurements at higher transverse momentum. Among the fragmentation models, the BCFY parametrization provides a better description of the experimental data than the PSSZ one, thanks to its harder spectrum at large p_T. Theoretical uncertainties remain sizable, with variations in the renormalization scale constituting the dominant contribution.

After validating the framework with HERA data, we generated predictions for D^0-meson production in UPCs at the LHC. The effect of electromagnetic dissociation is

incorporated in GγA-FONLL to model the survival probability of the photon-emitting nucleus and enable direct comparison with the UPC data. Various predictions for D^0 photoproduction in UPCs at the LHC, performed using the latest proton and nuclear PDF parametrizations and adopting different charm-quark mass hypotheses and fragmentation functions, were presented and discussed. The GγA-FONLL predictions obtained with both EPPS21 and nNNPDF3.0 nuclear PDFs provide a good description of the recent CMS measurement of the D^0 photonuclear cross section in UPCs across all p_T and rapidity intervals. In contrast, calculations based on the CT18ANLO proton PDF systematically overshoot the data, underscoring the importance of nuclear modifications. These effects are most pronounced for low-p_T D^0 mesons at forward rapidity, where low-x effects are expected to become more relevant. At high p_T, where nuclear effects are expected to be negligible, the GγA-FONLL predictions appear slightly softer than the data. The predictions presented in this paper also highlights the sensitivity of the predictions to the assumed charm-quark mass. While confirming the strong experimental and theoretical constraining power of charm production in UPCs, this study also underscores the need for further work to quantify competing effects, namely electromagnetic dissociation, possible modifications to charm-meson fragmentation, and uncertainties in the charm-quark mass. If left unaccounted for, these factors could bias the interpretation of low-x nuclear modifications.

In summary, the GγA-FONLL framework introduced here establishes a unified theoretical baseline for high-accuracy charm-photoproduction studies in both UPCs at the LHC, and in electron-ion collisions at the future Electron-Ion Collider. High-precision measurements across complementary regions of x and Q^2, together with comparisons to saturation-based approaches such as the color glass condensate [28,70], promise unprecedented insight into low-x gluon dynamics and the onset of gluon saturation.

ACKNOWLEDGMENTS

We thank Vadim Guzey, Mark Strikman, Petja Paakkinen, Ilkka Helenius, Cristian Baldenegro, Chris McGinn, Balázs Kovács, Spencer Klein for the fruitful discussions. G. M. I. is supported by the U.S. Department of Energy Grant No. DOE-SC0011088. A. M. S. is supported by the U.S. Department of Energy Grant No. DE-SC-0002145 and within the framework of the of the Saturated Glue (SURGE) Topical Theory Collaboration.

DATA AVAILABILITY

The data that support the findings of this article are openly available [71].

APPENDIX A: FIXED-ORDER CALCULATIONS FOR HERA

In Figs. 19–21 the fixed-order (FO) predictions for the rapidity and pseudorapidity distributions of D^{*+} mesons in electron-proton collisions at HERA are compared to the GγA-FONLL predictions and to the experimental data. The blue bands represent the renormalization-scale uncertainty of the FONLL calculation, whereas the gray bands correspond to the fixed-order (FO) result; the solid blue and dashed black curves denote their respective central predictions. The factorization scale is fixed at $\mu_F/\mu_0 = 1$. The PSSZ fragmentation parameter is set to $\varepsilon = 0.02$ for FONLL and $\varepsilon = 0.35$ for the FO calculation.

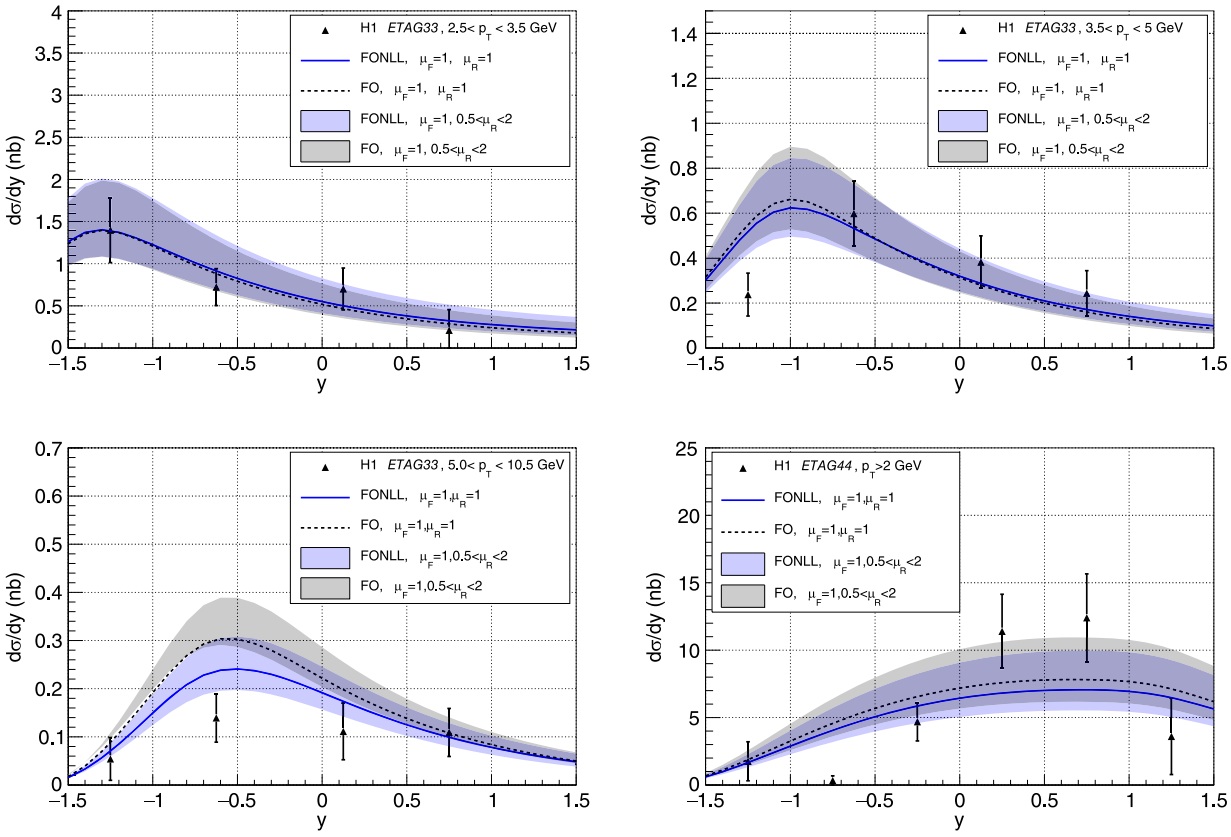

FIG. 19. Rapidity distribution of D^* mesons in photoproduction in electron-proton collisions at HERA. FONLL calculation [39] $\mu_F = \mu_R = 1$ (blue solid), FO calculation (black dashed). Shaded blue indicates variation of $0.5 < \mu_R < 2$ while $\mu_F = 1$ is fixed; shaded gray indicates renormalization scale variation for FO. PSSZ fragmentation function is used with $\varepsilon = 0.02$ for FONLL and $\varepsilon = 0.035$ for FO. Compared with data from H1 [29], for different p_T bins. Note different vertical scales. Positive rapidity is proton going direction.

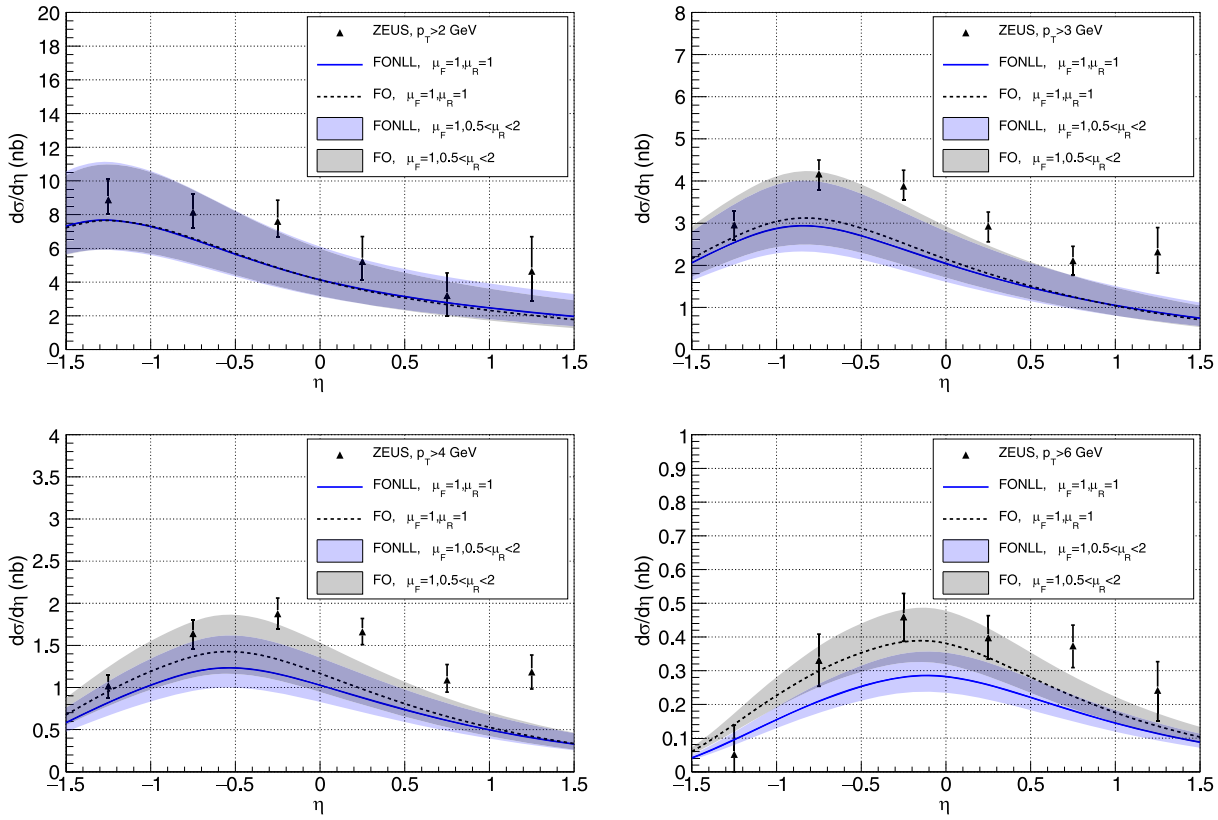

FIG. 20. Pseudorapidity distribution of D^* mesons in photoproduction in electron-proton collisions at HERA. FONLL calculation [39] $\mu_F = \mu_R = 1$ (blue solid), FO calculation (black dashed). Shaded blue indicates variation of $0.5 < \mu_R < 2$ while $\mu_F = 1$ is fixed; shaded gray indicates renormalization scale variation for FO. PSSZ fragmentation function is used with $\varepsilon = 0.02$ for FONLL and $\varepsilon = 0.035$ for FO. Compared with data from ZEUS [30], for different minimum p_T cuts: 2,3,4,6 GeV. Note different vertical scales. Positive pseudorapidity is proton direction.

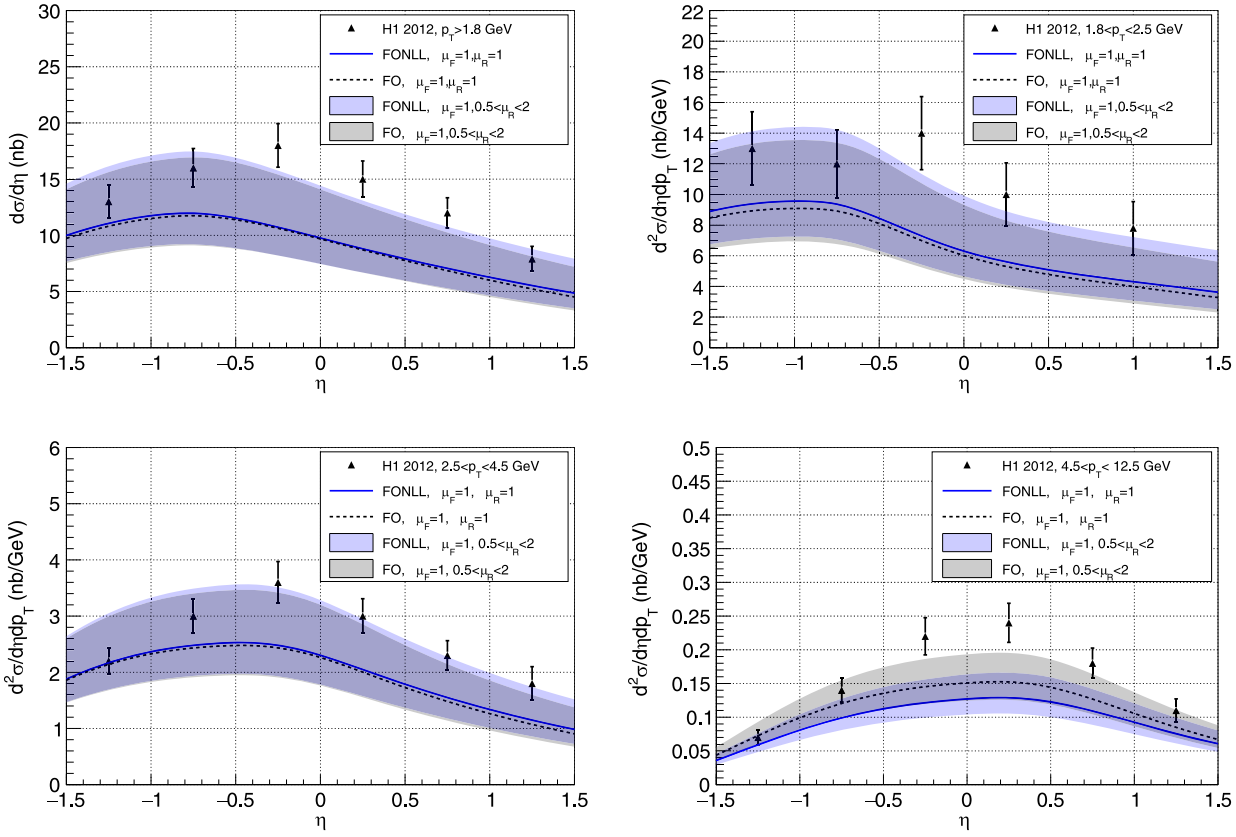

FIG. 21. Pseudorapidity distribution of D^* mesons in photoproduction in electron-proton collisions at HERA. FONLL calculation [39] $\mu_F = \mu_R = 1$ (blue solid), FO calculation (black dashed). Shaded blue indicates variation of $0.5 < \mu_R < 2$ while $\mu_F = 1$ is fixed; shaded gray indicates renormalization scale variation for FO. PSSZ fragmentation function is used with $\varepsilon = 0.02$ for FONLL and $\varepsilon = 0.035$ for FO. Compared with data from H1 [31], for different p_T bins. Note that data and results in three p_T bins (1.8,2.5), (2.5,4.5), (4.5,12.5) are presented as double differential cross sections. Positive pseudorapidity is proton direction.

APPENDIX B: SUPPLEMENTARY PREDICTIONS FOR UPC WITH NUCLEAR AND PROTON PDF

In Figs. 22 and 23 we present GγA-FONLL predictions for UPCs obtained with the EPPS21 (Fig. 22) and nNNPDF3.0 (Fig. 23) nuclear PDFs, shown as functions of the D^0 transverse momentum in several rapidity intervals. Figure 22 also includes the corresponding fixed-order (FO) calculation. Shaded bands represent systematic uncertainties from independent variations of the renormalization and factorization scales; for the FONLL curves the PDF uncertainty is displayed as well. The distributions are extended down to very low p_T, where both the scale-variation and PDF uncertainties become large. This sizable scale dependence is correlated with the PDF uncertainty, because at low p_T the calculation probes parton densities at low factorization scales, where the PDFs carry their largest intrinsic uncertainties. In Fig. 23, which shows the predictions obtained with the nNNPDF3.0 set, the uncertainty band at low p_T is slightly narrower than in the EPPS21 case, likely because the calculation employs a larger charm-quark mass and thus probes a

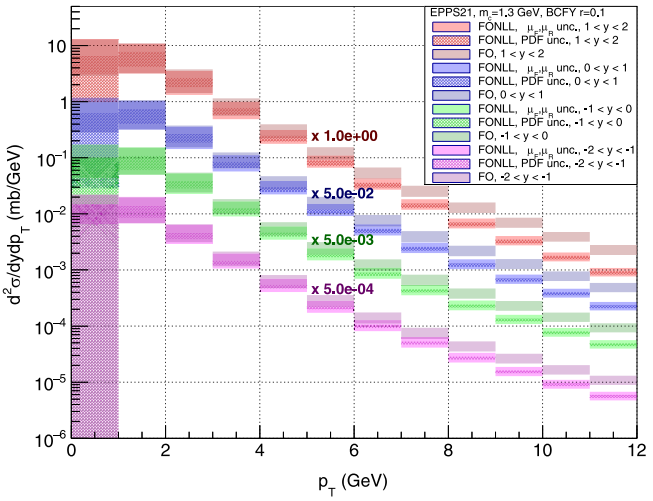

FIG. 22. Transverse momentum distribution for the D^0 production in UPC collisions at $\sqrt{s_{NN}} = 5.36$ TeV in four bins of rapidity: $(-2,-1), (-1,0), (0,1), (1,2)$. FONLL and FO calculation with EPPS21 nuclear PDF, charm mass $m_c = 1.3$ GeV with BCFY fragmentation function. Wider bands: factorization and renormalization scale variation, smaller (darker) bands: FONLL with PDF uncertainty.

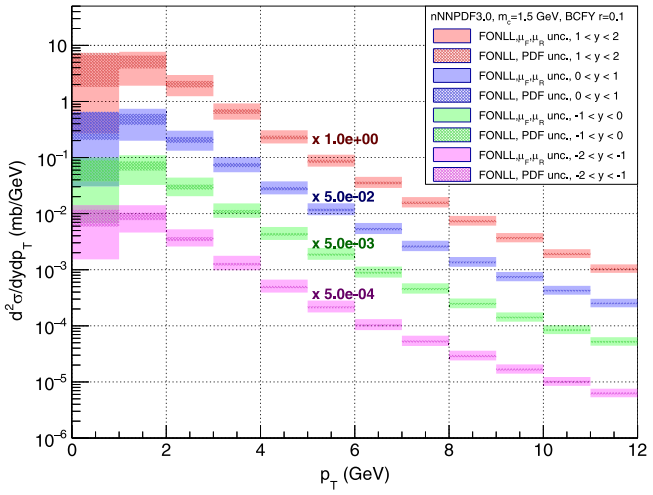

FIG. 23. Transverse momentum distribution for the D^0 production in UPC collisions at $\sqrt{s_{NN}} = 5.36$ TeV in four bins of rapidity: $(-2,-1),(-1,0),(0,1),(1,2)$. FONLL calculation with nNNPDF3.0 nuclear PDF, charm mass $m_c = 1.5$ GeV with BCFY fragmentation function. Wider bands: factorization and renormalization scale variation, smaller (darker) bands: PDF uncertainty.

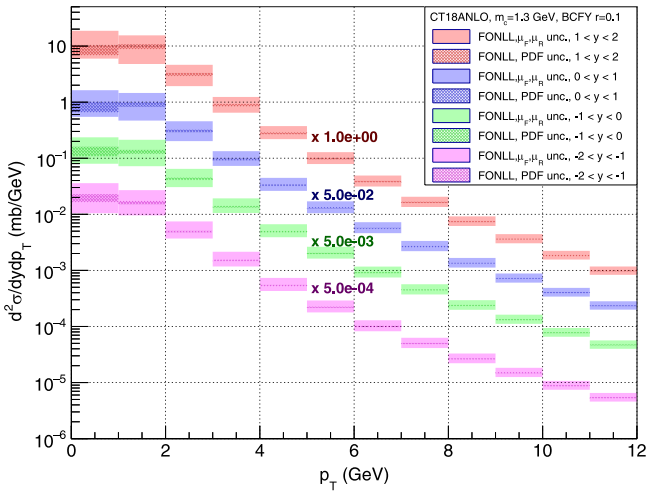

FIG. 24. Transverse momentum distribution for the D^0 production in UPC collisions at $\sqrt{s_{NN}} = 5.36$ TeV in four bins of rapidity: $(-2,-1),(-1,0),(0,1),(1,2)$. FONLL calculation with CT18ANLO proton PDF (scaled by $A = 208$), charm mass $m_c = 1.3$ GeV with BCFY fragmentation function. Wider bands: factorization and renormalization scale variation, smaller (darker) bands: PDF uncertainty.

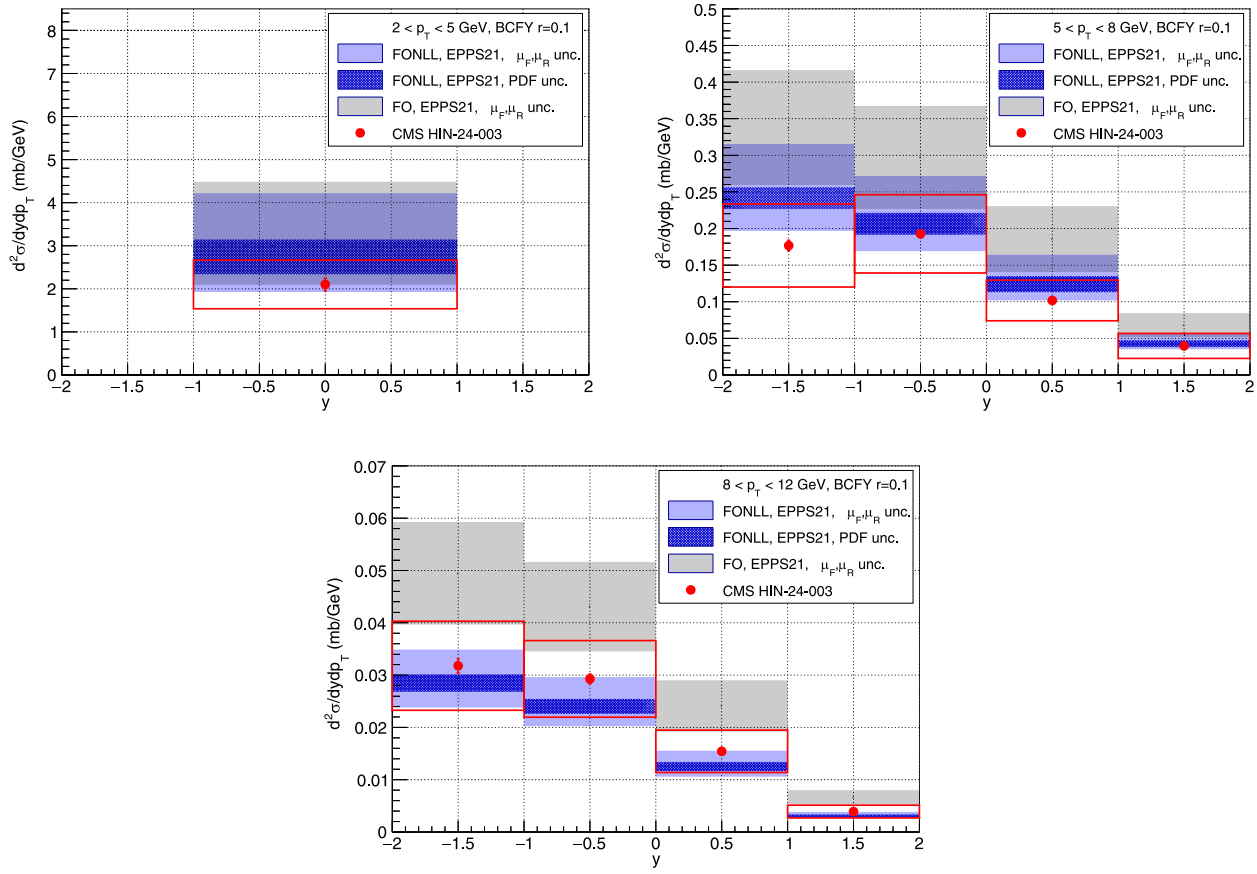

FIG. 25. Rapidity distribution for the D^0 production in UPC PbPb collisions at $\sqrt{s_{NN}} = 5.36$ TeV in p_T bins (2–5), (5–8), (8–12) GeV. Light blue band: FONLL calculation with factorization and renormalization scale variation, gray band: FONLL calculation with factorization and renormalization scale variation, dark blue band: FONLL EPPS21 [43] PDF uncertainty. Both FONLL and FO calculation done with BCFY fragmentation function [58,59] with parameter $r = 0.1$. Data are from CMS [32].

correspondingly higher renormalization and factorization scale.

In Fig. 24 we show the same distribution, this time evaluated with the proton CT18ANLO PDF and scaled by the mass number A, therefore without nuclear-shadowing effects. Scale-variation uncertainties at low p_T remain sizeble but are smaller than in the EPPS21 case, reflecting the tighter constraints on the proton PDFs. Figure 25 displays the rapidity distributions obtained with GγA-FONLL and fixed-order (FO) calculations based on EPPS21 and using the BCFY fragmentation function. The predictions are evaluated in the same p_T and y intervals as the CMS measurement to permit direct comparison with the data. Consistent with the pattern observed at HERA, the FO prediction lies slightly above the FONLL result at large p_T.

[1] Carlos A. Bertulani, Spencer R. Klein, and Joakim Nystrand, Physics of ultra-peripheral nuclear collisions, Annu. Rev. Nucl. Part. Sci. **55**, 271 (2005).

[2] Mark Strikman, Ramona Vogt, and Sebastian N. White, Probing small x parton densities in ultraperipheral AA and pA collisions at the LHC, Phys. Rev. Lett. **96**, 082001 (2006).

[3] A. J. Baltz, The physics of ultraperipheral collisions at the LHC, Phys. Rep. **458**, 1 (2008).

[4] E. Fermi, On the theory of the impact between atoms and electrically charged particles, Z. Phys. **29**, 315 (1924).

[5] Enrico Fermi, On the theory of collisions between atoms and electrically charged particles, Nuovo Cimento **2**, 143 (1925).

[6] C. F. von Weizsacker, Radiation emitted in collisions of very fast electrons, Z. Phys. **88**, 612 (1934).

[7] E. J. Williams, Nature of the high-energy particles of penetrating radiation and status of ionization and radiation formulae, Phys. Rev. **45**, 729 (1934).

[8] R. D. Ball and R. Keith Ellis, Heavy quark production at high-energy, J. High Energy Phys. 05 (2001) 053.

[9] Shreyasi Acharya *et al.*, Coherent J/ψ and ψ' photoproduction at midrapidity in ultra-peripheral Pb-Pb collisions at $\sqrt{s_{\rm NN}} = 5.02$ TeV, Eur. Phys. J. C **81**, 712 (2021).

[10] Shreyasi Acharya *et al.*, Energy dependence of coherent photonuclear production of J/ψ mesons in ultra-peripheral Pb-Pb collisions at $\sqrt{s_{\rm NN}} = 5.02$ TeV, J. High Energy Phys. 10 (2023) 119.

[11] Vardan Khachatryan *et al.*, Coherent J/ψ photoproduction in ultra-peripheral PbPb collisions at $\sqrt{s_{\rm NN}} = 2.76$ TeV with the CMS experiment, Phys. Lett. B **772**, 489 (2017).

[12] Armen Tumasyan *et al.*, Probing small bjorken-x nuclear gluonic structure via coherent J/ψ photoproduction in ultraperipheral Pb-Pb collisions at sNN = 5.02 TeV, Phys. Rev. Lett. **131**, 262301 (2023).

[13] R. Aaij *et al.*, Study of exclusive photoproduction of charmonium in ultra-peripheral lead-lead collisions, J. High Energy Phys. 06 (2023) 146.

[14] V. P. Goncalves and M. V. T. Machado, Vector meson production in coherent hadronic interactions: An update on predictions for RHIC and LHC, Phys. Rev. C **84**, 011902 (2011).

[15] V. P. Gonçalves, M. V. T. Machado, B. D. Moreira, F. S. Navarra, and G. Sampaio dos Santos, Color dipole predictions for the exclusive vector meson photoproduction in pp, pPb, and PbPb collisions at run 2 LHC energies, Phys. Rev. D **96**, 094027 (2017).

[16] V. Guzey, E. Kryshen, and M. Zhalov, Coherent photoproduction of vector mesons in ultraperipheral heavy ion collisions: Update for run 2 at the CERN Large Hadron Collider, Phys. Rev. C **93**, 055206 (2016).

[17] V. Guzey, M. Strikman, and M. Zhalov, Accessing transverse nucleon and gluon distributions in heavy nuclei using coherent vector meson photoproduction at high energies in ion ultraperipheral collisions, Phys. Rev. C **95**, 025204 (2017).

[18] Kari J. Eskola, Christopher A. Flett, Vadim Guzey, Topi Löytäinen, and Hannu Paukkunen, Exclusive J/ψ photoproduction in ultraperipheral Pb + Pb collisions at the CERN Large Hadron Collider calculated at next-to-leading order perturbative QCD, Phys. Rev. C **106**, 035202 (2022).

[19] Jan Cepila, Jesus Guillermo Contreras, and Michal Krelina, Coherent and incoherent J/ψ photonuclear production in an energy-dependent hot-spot model, Phys. Rev. C **97**, 024901 (2018).

[20] B. Z. Kopeliovich, M. Krelina, J. Nemchik, and I. K. Potashnikova, Ultraperipheral nuclear collisions as a source of heavy quarkonia, Phys. Rev. D **107**, 054005 (2023).

[21] Heikki Mäntysaari and Björn Schenke, Probing subnucleon scale fluctuations in ultraperipheral heavy ion collisions, Phys. Lett. B **772**, 832 (2017).

[22] Björn Schenke, Heikki Mäntysaari, Farid Salazar, Chun Shen, and Wenbin Zhao, Vector meson production in ultraperipheral heavy ion collisions, in *Proceedings of the 1st International Workshop on the physics of Ultra Peripheral Collisions* (2024).

[23] Adeola Adeluyi, C. A. Bertulani, and M. J. Murray, Nuclear effects in photoproduction of heavy quarks and vector mesons in ultraperipheral PbPb and pPb collisions at the LHC, Phys. Rev. C **86**, 047901 (2012).

[24] Adeola Adeluyi and C. A. Bertulani, Constraining gluon shadowing using photoproduction in ultraperipheral pA and AA collisions, Phys. Rev. C **85**, 044904 (2012).

[25] Spencer R. Klein, Joakim Nystrand, and Ramona Vogt, Heavy quark photoproduction in ultraperipheral heavy ion collisions, Phys. Rev. C **66**, 044906 (2002).

[26] V. P. Goncalves and C. A. Bertulani, Peripheral heavy ion collisions as a probe of the nuclear gluon distribution, Phys. Rev. C **65**, 054905 (2002).

[27] V. P. Goncalves and M. V. T. Machado, The QCD pomeron in ultraperipheral heavy ion collisions. 3, Photonuclear production of heavy quarks, Eur. Phys. J. C **31**, 371 (2003).
[28] Patricia Gimeno-Estivill, Tuomas Lappi, and Heikki Mäntysaari, Inclusive D^0 photoproduction in ultraperipheral collisions, Phys. Rev. D **111**, 114036 (2025).
[29] C. Adloff *et al.*, Measurement of D* meson cross sections at HERA and determination of the gluon density in the proton using NLO QCD, Nucl. Phys. **B545**, 21 (1999).
[30] J. Breitweg *et al.*, Measurement of inclusive $D^{*\pm}$ and associated dijet cross-sections in photoproduction at HERA, Eur. Phys. J. C **6**, 67 (1999).
[31] F. D. Aaron *et al.*, Measurement of inclusive and Dijet D* meson cross sections in photoproduction at HERA, Eur. Phys. J. C **72**, 1995 (2012).
[32] CMS Collaboration, Constraining nuclear parton dynamics with the first measurement of D0-photoproduction in ultra-peripheral heavy-ion collisions at the LHC, Report No. CMS-PAS-HIN-24-003, 2024.
[33] A. Accardi *et al.*, Electron ion collider: The next QCD frontier: Understanding the glue that binds us all, Eur. Phys. J. A **52**, 268 (2016).
[34] R. Abdul Khalek *et al.*, Science requirements and detector concepts for the electron-ion collider: EIC Yellow report, Nucl. Phys. **A1026**, 122447 (2022).
[35] J. L. Abelleira Fernandez *et al.*, A large hadron electron collider at CERN: Report on the physics and design concepts for machine and detector, J. Phys. G **39**, 075001 (2012).
[36] P. Agostini *et al.*, The large hadron–electron collider at the HL-LHC, J. Phys. G **48**, 110501 (2021).
[37] Matteo Cacciari, Mario Greco, and Paolo Nason, The p_T spectrum in heavy-flavour hadroproduction. J. High Energy Phys. 05 (1998) 007.
[38] Matteo Cacciari, Stefano Frixione, and Paolo Nason, The p(T) spectrum in heavy flavor photoproduction, J. High Energy Phys. 03 (2001) 006.
[39] Stefano Frixione and Paolo Nason, Phenomenological study of charm photoproduction at HERA, J. High Energy Phys. 03 (2002) 053.
[40] L. Frankfurt, V. Guzey, and M. Strikman, Leading twist nuclear shadowing phenomena in hard processes with nuclei, Phys. Rep. **512**, 255 (2012).
[41] R. Keith Ellis and P. Nason, QCD radiative corrections to the photoproduction of heavy quarks, Nucl. Phys. **B312**, 551 (1989).
[42] J. Smith and W. L. van Neerven, QCD corrections to heavy flavor photoproduction and electroproduction, Nucl. Phys. **B374**, 36 (1992).
[43] Kari J. Eskola, Petja Paakkinen, Hannu Paukkunen, and Carlos A. Salgado, EPPS21: A global QCD analysis of nuclear PDFs, Eur. Phys. J. C **82**, 413 (2022).
[44] Rabah Abdul Khalek, Rhorry Gauld, Tommaso Giani, Emanuele R. Nocera, Tanjona R. Rabemananjara, and Juan Rojo, nNNPDF3.0: Evidence for a modified partonic structure in heavy nuclei, Eur. Phys. J. C **82**, 507 (2022).
[45] Tie-Jiun Hou *et al.*, New CTEQ global analysis of quantum chromodynamics with high-precision data from the LHC, Phys. Rev. D **103**, 014013 (2021).
[46] Kari J. Eskola, Petja Paakkinen, Hannu Paukkunen, and Carlos A. Salgado, EPPS16: Nuclear parton distributions with LHC data, Eur. Phys. J. C **77**, 163 (2017).
[47] Rabah Abdul Khalek, Jacob J. Ethier, Juan Rojo, and Gijs van Weelden, nNNPDF2.0: Quark flavor separation in nuclei from LHC data, J. High Energy Phys. 09 (2020) 183.
[48] H. Abramowicz *et al.*, Combination of measurements of inclusive deep inelastic $e^{\pm}p$ scattering cross sections and QCD analysis of HERA data, Eur. Phys. J. C **75**, 580 (2015).
[49] Rabah Abdul Khalek, Jacob J. Ethier, and Juan Rojo, Nuclear parton distributions from lepton-nucleus scattering and the impact of an electron-ion collider, Eur. Phys. J. C **79**, 471 (2019).
[50] Stefano Frixione, Michelangelo L. Mangano, Paolo Nason, and Giovanni Ridolfi, Improving the Weizsacker-Williams approximation in electron—proton collisions, Phys. Lett. B **319**, 339 (1993).
[51] Carlos A. Bertulani and Gerhard Baur, Electromagnetic processes in relativistic heavy ion collisions, Phys. Rep. **163**, 299 (1988).
[52] Kari J. Eskola, Vadim Guzey, Ilkka Helenius, Petja Paakkinen, and Hannu Paukkunen, Spatial resolution of dijet photoproduction in near-encounter ultraperipheral nuclear collisions, Phys. Rev. C **110**, 054906 (2024).
[53] J. Nystrand, Electromagnetic interactions in nucleus-nucleus and proton-proton collisions, Nucl. Phys. **A752**, 470 (2005).
[54] V. Guzey and M. Klasen, Inclusive dijet photoproduction in ultraperipheral heavy ion collisions at the CERN Large Hadron Collider in next-to-leading order QCD, Phys. Rev. C **99**, 065202 (2019).
[55] Anthony J. Baltz, Spencer R. Klein, and Joakim Nystrand, Coherent vector meson photoproduction with nuclear breakup in relativistic heavy ion collisions, Phys. Rev. Lett. **89**, 012301 (2002).
[56] Petja Paakkinen, Kari J. Eskola, Vadim Guzey, Ilkka Helenius, and Hannu Paukkunen, Collision geometry in UPC dijet production, Phys. Proc. UPC **1**, 16 (2024).
[57] C. Peterson, D. Schlatter, I. Schmitt, and Peter M. Zerwas, Scaling violations in inclusive e^+e^- annihilation spectra, Phys. Rev. D **27**, 105 (1983).
[58] Eric Braaten, King-man Cheung, Sean Fleming, and Tzu Chiang Yuan, Perturbative QCD fragmentation functions as a model for heavy quark fragmentation, Phys. Rev. D **51**, 4819 (1995).
[59] Matteo Cacciari and Paolo Nason, Charm cross-sections for the Tevatron Run II, J. High Energy Phys. 09 (2003) 006.
[60] Matteo Cacciari, Stefano Frixione, Nicolas Houdeau, Michelangelo L. Mangano, Paolo Nason, and Giovanni Ridolfi, Theoretical predictions for charm and bottom production at the LHC, J. High Energy Phys. 10 (2012) 137.
[61] Stefano Frixione, Michelangelo L. Mangano, Paolo Nason, and Giovanni Ridolfi, Total cross-sections for heavy flavor production at HERA, Phys. Lett. B **348**, 633 (1995).
[62] Stefano Frixione, Paolo Nason, and Giovanni Ridolfi, Differential distributions for heavy flavor production at HERA, Nucl. Phys. **B454**, 3 (1995).

[63] B. A. Kniehl, G. Kramer, I. Schienbein, and H. Spiesberger, Inclusive photoproduction of $D^{*\pm}$ mesons at next-to-leading order in the general-mass variable-flavor-number scheme, Eur. Phys. J. C **62**, 365 (2009).
[64] G. Kramer and H. Spiesberger, Inclusive photoproduction of D* mesons with massive charm quarks, Eur. Phys. J. C **38**, 309 (2004).
[65] Matteo Cacciari and Mario Greco, Large p_T hadroproduction of heavy quarks, Nucl. Phys. **B421**, 530 (1994).
[66] P. Aurenche, J. P. Guillet, and M. Fontannaz, Parton distributions in the photon, Z. Phys. C **64**, 621 (1994).
[67] E. Reya M. Glück and A. Vogt, Photonic parton distributions, Phys. Rev. D **46**, 1973 (1992).
[68] L. V. Gribov, E. M. Levin, and M. G. Ryskin, Semihard processes in QCD, Phys. Rep. **100**, 1 (1983).
[69] J. Rausch, V. Guzey, and M. Klasen, Numerical evaluation of the nonlinear Gribov-Levin-Ryskin-Mueller-Qiu evolution equations for nuclear parton distribution functions, Phys. Rev. D **107**, 054003 (2023).
[70] Edmond Iancu and Raju Venugopalan, *The Color Glass Condensate and High-Energy Scattering in QCD* (World Scientific, 2003), pp. 249–3363.
[71] Matteo Cacciari, Gian Michele Innocenti and Anna M. Staśto Inclusive open charm photoproduction in ultra-peripheral collisions at the LHC with GγA-FONLL, arXiv:2506.09893.